DISSERTATIONES
PHYSICAE
UNIVERSITATIS
TARTUENSIS
104

RASMUS TALVISTE

Atmospheric-pressure He plasma jet: effect of dielectric tube diameter

DISSERTATIONES PHYSICAE UNIVERSITATIS TARTUENSIS
104

DISSERTATIONES PHYSICAE UNIVERSITATIS TARTUENSIS
104

RASMUS TALVISTE

Atmospheric-pressure He plasma jet: effect of dielectric tube diameter

UNIVERSITY OF TARTU
Press

This study was carried out at the Institute of Physics, University of Tartu. This dissertation was admitted on May 23rd 2016 in partial fulfillment of the requirements for the degree of Doctor of Philosophy in physics was allowed for defence by the Science Council of the Institute of Physics, University of Tartu.

Supervisor: PhD Indrek Jõgi, University of Tartu

Opponents: PhD Assoc. Prof. Karol Hensel, Comenius University, Bratislava, Slovakia

Defence: October 14, 2016 at the University of Tartu

The research presented in this thesis has been supported by the Estonian Science Foundation project no. ETF9310 and graduate school "Functional materials and technologies".

ISSN 1406-0647
ISBN 978-9949-77-219-3 (print)
ISBN 978-9949-77-220-9 (pdf)

University of Tartu Press
www.tyk.ee

TABLE OF CONTENTS

LIST OF ORIGINAL PUBLICATIONS

CC-level publications related to atmospheric pressure plasma physics:

I. I. Jõgi, R. Talviste, J. Raud, K. Piip and P. Paris. (2014) "The influence of the tube diameter on the properties of an atmospheric pressure He micro-plasma jet". *Journal of Physics D: Applied physics,* **47**, 415202

II. R. Talviste, I. Jõgi, J. Raud and P. Paris. (2016) "Development of ionization waves in an atmospheric-pressure micro-plasma jet". *Contributions to plasma physics,* **56**, 101002

III. R. Talviste, I. Jõgi, J. Raud and P. Paris. (2016) "The effect of dielectric tube diameter on the propagation velocity of ionization waves in a He atmospheric-pressure micro-plasma jet". *Journal of Physics D: Applied physics,* **49**, 195201

Other CC-level publications:

1. T. Tätte. M. Part, R. Talviste, K. Hanschmidt, K. Utt, U. Mäeorg, I. Jõgi, V. Kiisk, H. Mändar, G. Nurk and P. Rauwell. (2014) "Yttria stabilized zirconia microtubes for microfluidics under extreme conditions". *RSC advances,* **34**, 101039

2. T. Tätte, M. Paalo, M. Part, R. Talviste, V. Kiisk, H. Mändar, K. Põhako, T. Pehk, K. Reivelt, M. Natali, J. Gurauskis, A. Lõhmus and U. Mäeorg. (2011) "Alkoxide-based precursors for direct drawing of metal oxide micro- and nanofibers". *Science and Technology of Advanced Materials*, **12**, 034412

3. T. Tätte A. Kolesnikova, M. hussainov, R. Talviste, R. Lõhmus, A. Romanov, I. Hussainova and A. Lõhmus. (2010) "Crack formation during post-treatment of nano- and microfibers by sol-gel technique". *Journal of Nanoscience and Nanotechnology*, **10**, 101166

Author's contribution

The author conducted most of the experimental work in articles **I**, **II** and **III**. The author participated in data analysis and writing of article **I**, conducted most of the data analysis of paper **II** and participated in writing of article **II**. Most of the data analysis and writing of article **III** was done by the author.

ABBREVIATIONS

APPJ	Atmospheric pressure plasma jet
CAP	Cold atmospheric plasma
CRM	Collisional radiative model
DC	Direct current
EEDF	Electron energy distribution function
FNS	First negative system of N_2
FWHM	Full width at half maximum
LTE	Local thermodynamic equilibrium
PLTE	Partial local thermodynamic equilibrium
RNS	Reactive nitrogen species
ROS	Reactive oxygen species
SPS	Second positive system of N_2
TE	Thermodynamic equilibrium
VOC	Volatile organic compound

1. INTRODUCTION

Non-equilibrium atmospheric pressure plasma jet (APPJ) is a promising plasma source that has been actively investigated during the past decade [1–3]. The motivation behind the intensive research is the non-equilibrium or "cold" nature of these devices which enables a vast variety of applications where gas temperature has to remain close to room temperature. First and foremost, APPJs have been employed in biomedicine for sterilization [4], wound healing [5, 6] and recently for cancer treatment [7, 8]. Some additional applications of APPJs include surface treatment [9] and modification [10] of temperature sensitive non-biological materials and nanomaterial synthesis [11].

An APPJ device typically consists of a dielectric tube with a powered electrode wrapped around the tube or inserted into the tube. A noble gas such as Ar or He is fed into the tube and plasma is ignited by applying sinusoidal or pulsed voltage of several kilovolts with excitation frequencies varying from several hundred hertz to gigahertz. An APPJ working in the kHz frequency range appears continuous to the eye but actually consists of discrete highly luminous travelling plasma fronts which have also been referred to as "plasma bullets" [12] which propagate with velocities of up to 10^3 km/s. Several other terms for this phenomena have been proposed in literature such as ionization wave, plasma front and guided streamer.

The application of APPJs in biomedicine requires precise control over plasma parameters. It has been shown that the propagation velocity of the ionization wave and the spatio-temporal behavior of plasma parameters such as electron density, electron temperature, gas temperature, density of ions and various excited species are influenced by externally controllable parameters such as the voltage characteristics, gas type and flow rate and the electrode configuration of the APPJ device.

Additionally, the diameter of the dielectric tube can influence plasma parameters for example the electron concentration and temperature. Most common is the use of quartz tubes with inner diameter in range of several millimeters and wall thickness of 0.5–2 mm [3]. Reducing the tube diameter below the millimeter range could have inherent advantages at specific applications. Firstly, the small spatial dimensions of the plasma jet can result in better spatial resolution of plasma treatment at hand. Secondly, increased departure from thermodynamic equilibrium [13, 14] i.e. higher electron temperature and lower gas temperature can be expected due to the increased diffusion losses to the walls. Thirdly, it is noteworthy that the well-known Pachen minimum for electrical breakdown between two plane electrodes at atmospheric pressure occurs at the sub-millimeter range.

The possible effect of the dielectric tube on important plasma parameters (electron concentration, gas temperature, ionization wave velocity) has received little attention except a few computational studies and experimental works in a dielectric capillary in air flow [15, 16]. It was shown in air plasmas that the ionization wave velocity increases with decreasing tube diameter and has a

maximum at 100 μm and decreases in even smaller diameter tubes [16]. The effect of dielectric tube parameters such as the diameter, wall thickness and dielectric constant in APPJs in noble gases has not been explicitly studied before this thesis.

This thesis can be divided into four parts each with its own sub-goals. The aim of the first part was to clarify the effect of external parameters such as applied voltage, voltage polarity and gas flow rate and the spatio-temporal behavior of the ionization wave for the APPJ in a 500 μm tube. The aim of the second part was to determine the effect of tube diameter in the range of 80–500 μm on the ionization wave velocity and its spatio-temporal behavior inside the quartz tube and in the He jet emerging into ambient air. The goal of the third part was to determine the effect tube diameter in the range of 80–500 μm on the plasma sustaining voltage. The aim of the fourth part of the thesis was to spectroscopically determine essential plasma parameters electron density, gas temperature and He excitation temperature. Finally, several experiments were conducted with Y-ZrO_2 microtubes to determine whether the dielectric tube material substantially influences the plasma parameters.

2. SCIENTIFIC BACKGROUND

2.1. Atmospheric pressure plasma jets

2.1.1. Main features of APPJs

Atmospheric pressure plasma jets (APPJs) are plasma sources that produce cold non-equilibrium plasma typically in a noble gas flow through a dielectric tube into ambient air [3]. The confinement of the plasma inside of the noble gas jet is caused by much larger ionization rate of noble gas compared to the ambient air surrounding the jet [3]. APPJs appear continuous when viewed with naked eye or taking time averaged photographs like on figure 4.2. However, temporally resolved imaging reveals that one or several fast moving ionization waves with the duration of several hundred nanoseconds pass through the dielectric tube and noble gas jet every half-period [17] or per applied voltage pulse [18]. These ionization waves are highly luminous and move with velocity in the range of $10–10^3$ km/s which is several orders of magnitude higher than gas flow rate [3]. They have been termed as "plasma bullets" [1], "guided streamers "[19] and "guided ionization waves" [3].

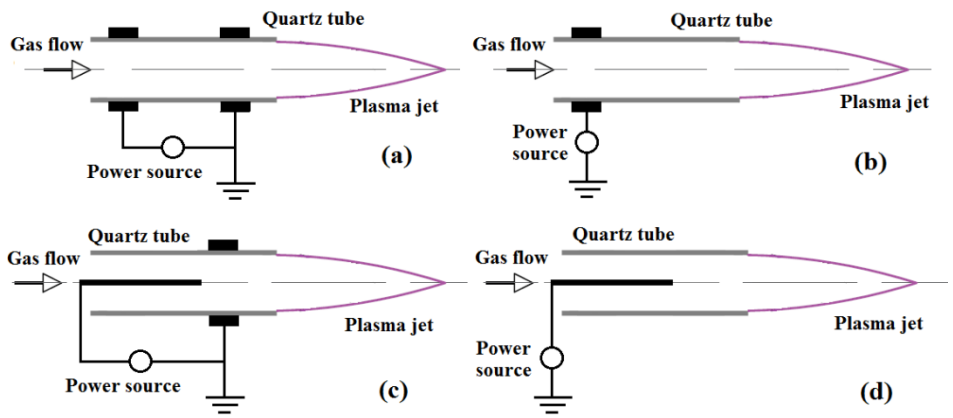

Figure 2.1. Various electrode configurations utilized in APPJs.

Figure 2.1 shows the various electrode geometries that have been utilized in APPJs including DBD jets, DBD-like jets and single electrode jets [20]. Typically the high-voltage electrode is either ring-shaped wrapped around the dielectric tube or a thin rod inserted in the tube resulting in linear-field and cross-field APPJs, respectively [21]. It is proposed [21] that the advantage of the linear-field geometry is the more efficient transport of active species to the treated substrate.

The characteristics of APPJs are determined by externally controllable parameters like applied voltage amplitude, shape and polarity, repetition frequency, gas flow rate and the dielectric tube diameter and material. Properties and behavior of the ionization waves, the length of the plasma jet and also several key plasma parameters such as discharge current, electron density, electron temperature, excitation temperature, gas temperature, density of ions and active radical species are determined by the operation conditions of the APPJ.

An important characteristic of APPJs is the plasma ignition voltage. Direct current (dc) pulsed and sinusoidal (ac) voltages in several frequency ranges (kHz, MHz and GHz) are most commonly employed. The dc pulsed excitation employs fast pulse rise times on the order of some tens of nanoseconds that results in over-voltage breakdown and the voltage amplitude has been seen to strongly affect the propagation of the ionization wave [3, 12]. In the case of the sinusoidal voltage with kHz frequencies, the applied voltage changes slowly in time ($\Delta V/\Delta t$) and during the short time of breakdown and ionization wave propagation (~few hundred nanoseconds) the voltage remains practically constant. The repetition frequency may affect the concentrations of species that decay with time such as electrons, ions, radical and metastables [3, 22]. Polarity of the applied voltage has been shown to effect the temporal behavior of the ionization waves and the radial distribution of active species [23].

The gas flow rate determines whether the flow is laminar or turbulent. It has been shown that the dimensionless plasma jet length (length/diameter) in He depends on the Reynolds number (*Re*) [24]. The dimensionless Reynolds number characterizes the measure of inertial to viscous forces and is given by

$$Re = {(\rho \cdot V \cdot D)}/{\mu}, \quad (1)$$

where ρ and μ are respectively the density and viscosity, V is the linear gas flow velocity and D is the tube diameter. The dimensionless length of the plasma jet increases with Re value up to the Re values 200–250 where the transition to turbulent regime occurs and the length decreases.

2.1.2. Dielectric tube

The influence of dielectric tube on the discharge characteristics and plasma parameters in APPJs has not been extensively studied. There are three important characteristics of the dielectric tube: the inner radius of the tube, the relative permittivity of the tube material and the wall thickness. Most often the APPJs are ignited in quartz tubes with inner diameters in the range of a few millimeters and wall thickness around 1 mm [3].

There exist a few theoretical and experimental works where the effect of dielectric tube diameter was studied in an air discharge in a capillary [15, 16] and several modelling studies in He [25, 26, 27]. The reduction of the physical plasma dimensions affects the plasma ignition voltage. The most well-known is

the breakdown between two parallel plate electrodes where the breakdown voltage V_b dependence on the similarity parameter ($p \cdot d$) is called the Paschen curve [28, 29]

$$V_b = \frac{B(pd)}{C + \ln(pd)}, \tag{2}$$

where B and C are constants, p is the pressure and d is the gap between the electrodes. These curves exhibit a minimum depending on the gas and electrode material. For atmospheric pressures this minimum corresponds to sub-millimeter gap size. In air plasma confined to the dielectric tube, it has been shown that reducing the tube diameter down to 100 μm increases the propagation velocity of the ionization wave and further reduction of the diameter decreases the velocity [15, 16].

The relative permittivity of the dielectric has been shown to change the axial Laplacian electric field distribution [15, 25]. Furthermore in a modelling study in air an increase of ε_r by an order of magnitude (from 1 to 10) resulted in a decreased velocity and an increased maximum electron density [15].

Up to date no studies have been reported on the possible effect of tube wall thickness. It is expected that the tube wall thickness influences the capacity and might affect the breakdown voltage and possibly the velocity of the ionization wave. Both the tube thickness and dielectric constant of the tube could also possibly have an effect on the deposited surface charge on the inner walls of the tube.

The following chapters give a short overview of the main topics connected with the characteristics of APPJ-s investigated in the present study. The ignition and sustaining voltage of the discharge as well as the velocity of ionization waves are connected to the gas breakdown and subsequent development of ionization waves. The plasma characteristics, i.e. the electron density as well as electron, gas and excitation temperatures are influenced by the ionization waves but also by the deviation of plasma from the thermodynamic equilibrium. Finally, the importance of non-equilibrium plasma of APPJ in plasma chemistry is explained and main applications are given.

2.2. Gas breakdown and ionization waves

2.2.1. Electron avalanches and breakdown mechanisms

Breakdown in gas discharges proceeds via two different mechanisms: Townsend and spark breakdown mechanisms. For both mechanisms the breakdown is initiated with the formation of electron avalanches which is the exponential multiplication of electrons in the strong electric field E. This multiplication of electrons per unit distance is in the case of uniform electric field

$$n_e(x) = n_{e0} \cdot \exp(\alpha \cdot x), \tag{3}$$

where n_{e0} is the initial electron concentration, n_e is the electron concentration and α is the first Townsend ionization coefficient which is a strong function of the reduced electric field E/N where N is number density of gas. The development of an avalanche is depicted on figure 2.2. A single free electron produced in the gas gap is accelerated in the direction opposite to the applied electric field E_0. As the velocity of the electron increases and it collides with neutral gas atoms it ionizes them by kicking out new electrons. Electron density in the avalanche head follows a Gaussian distribution and the ion concentration in the trail of the avalanche grows exponentially while radially it is also Gaussian.

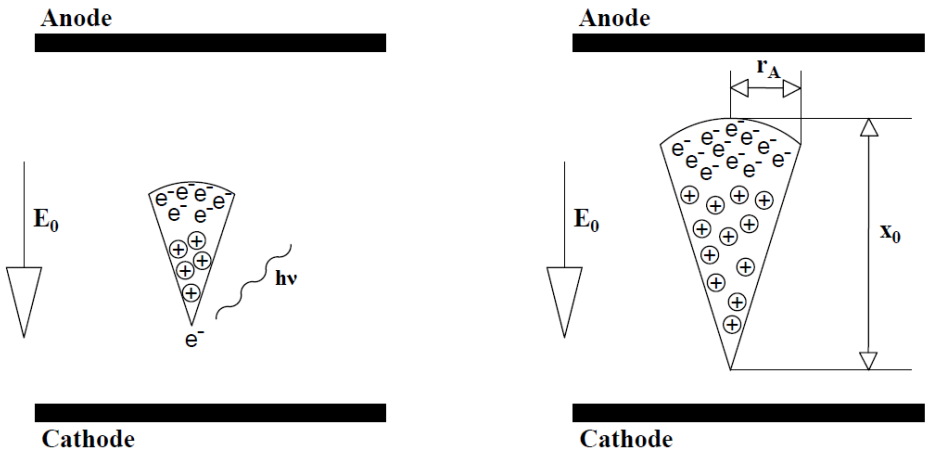

Figure 2.2. Avalanche formation as a result of a primary electron. Left hand illustrates the start of an avalanche and right hand side figure the avalanche growth and the relevant parameters.

Ions and photons created in the avalanche give rise to secondary electron emission from the cathode which start new avalanches. At sufficiently strong electric fields, this will lead to the Townsend breakdown mechanism which is a uniform breakdown of the gas gap dependent on the secondary emission from the cathode with breakdown condition given by

$$\alpha \cdot d = \ln(\frac{1}{\gamma} + 1). \quad (4)$$

Here d is the gap size and γ is the secondary electron emission coefficient, which depends on the cathode material, surface conditions, the gas type and the reduced electric field E/N. The voltage where this condition is met and breakdown occurs is the breakdown voltage V_b given by Paschen criteria (1). The Townsend mechanism dominates at small over-voltages and $p{\cdot}d$ values below 200 Torr·cm [29].

At high over-voltages or large $p \cdot d$ values a change in the avalanche behavior takes place because the large amplification of the electron number $N_e \approx \exp(\alpha x)$ results in the creation of a significant space charge. At some critical value of the number of electrons

$$N_e \approx \exp(\alpha x) \approx 3*10^8 \ (\alpha x \geq 20) \tag{5}$$

the space charge electric field E_A becomes equal to E_0. This is known as the Meek breakdown condition or the streamer formation criterion.

There are two important points to note. Firstly, at the Meek breakdown criterion the avalanche radius is roughly equal to characteristic ionization length $1/\alpha$ and the increase in transverse radius slows down. Secondly, the non-uniformity of electric field affects the breakdown condition since it is the ionization integral $N_e = \int_{x_1}^{x_2} \alpha(E)dx$ that has to exceed the threshold value. Since $\alpha(E) \sim \exp(E)$ stronger local electric field results in exponentially higher ionization and the breakdown condition has to be met only at a limited space region for the streamer to occur, for example as in corona discharge with enhanced electric field near the sharp tip.

2.2.2. Streamer propagation models, positive and negative streamers

A positive streamer is formed usually near the anode when the Meek criterion is met. The propagation of the self-sustained positive or cathode directed streamer is depicted on right hand side of figure 2.3. High-energy photons from the primary avalanche or streamer head provide seed electrons for secondary avalanches which form in the space charge electric field. These secondary avalanches are pulled into the positive streamer head neutralizing it, forming a quazi-neutral streamer channel and leaving behind a new positive space charge. As a result of this repeated process the streamer propagates towards the cathode with velocity in air at atmospheric pressure 10^8 cm/s which corresponds to electron drift velocity in the electric field space charge at the streamer head [28, 29].

There exist two models for the description of the propagation of a self-sustaining positive streamer. One model was proposed by Dawson and Winn in 1965 [30] and it describes the autonomous propagation of the streamer independently of the external electric field of the anode with the assumption of very low conductivity of the streamer channel. The model assumes that when the secondary avalanches reach the streamer head the number of charges and the radius of the avalanche and streamer head become equal. The positive space charge is then neutralized by the electrons of the avalanche. The electric field in the streamer head remains constant according to this model.

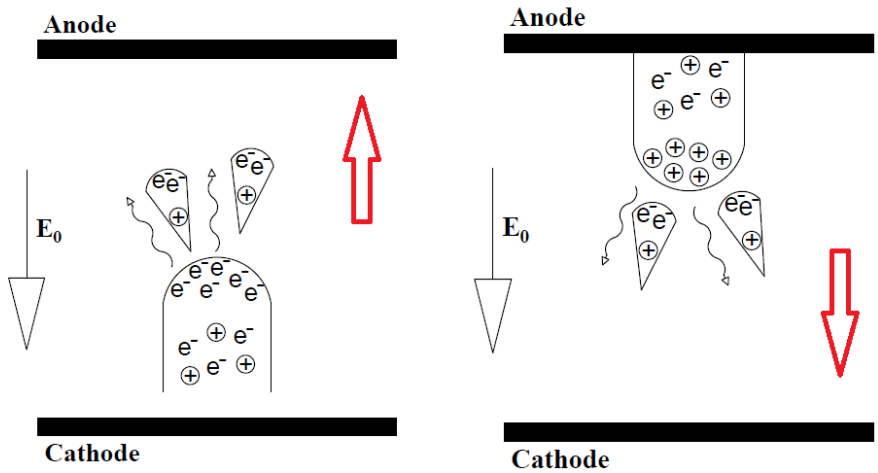

Figure 2.3. Propagation of an anode directed negative streamer (left) and a cathode directed positive streamer (right). Also shown is the direction of the Laplacian electric field and streamer propagation direction (red arrows).

A different model has been proposed by Klingbeil [31] and Lozansky and Firsov [32] which considers the streamer channel as an ideal conductor connected to the anode. The streamer channel is viewed as an anode extension and the streamer propagation takes place due to electron drift in the maximum electric field E_{max} located at the tip of the streamer which is given by

$$\frac{E_{max}}{E_0} = 3 + \left(\frac{l}{r}\right)^{0.92}, \tag{6}$$

where l and r are the streamer length and radius, respectively. The increase of E_{max} with the streamer length should also lead to increased electron drift velocity. It is noteworthy that in APPJs the conductive channel has a finite resistance [19] and both of the models are expected to be somewhat inaccurate.

The formation of a negative or anode directed streamer takes place in the gap at the same condition as the positive streamer (E_a~E_0). The mechanism of propagation is similar and is shown in left hand side of figure 2.3. Secondary avalanches are again initiated by photoionization due to high-energy photons from the primary avalanche. Different in this case is that the propagation direction of secondary avalanches is in the same direction as the streamer propagation. The streamer propagation occurs as the neutralization of the positive tails of secondary avalanches by the negatively charged streamer head.

2.2.3. Ionization waves in APPJs

Both Townsend and Spark breakdown mechanisms can occur in APPJs depending on the electrode configuration. The Townsend breakdown is expected to occur with configurations shown on figure 2.1a and 2.1c while the configuration of 2.1b and 2.1d should lead to spark breakdown.

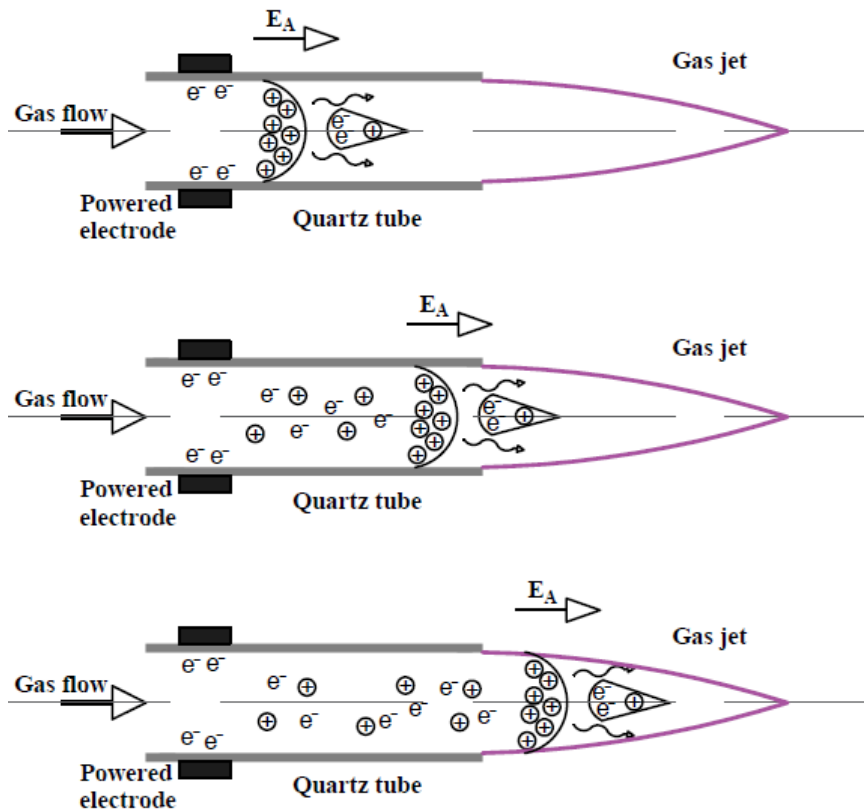

Figure 2.4. Propagation of the ionization front in an APPJ from top to bottom. E_A is the space charge electric field direction.

The propagation mechanism for ionization waves in APPJs was initially proposed by Lu and Laroussi [1] and later developed by Karakas *et al* [33]. It is very similar to that of streamers. The propagation of a positive guided ionization wave is shown on figure 2.4 together with the space charge electric field direction. The propagation is caused by the acceleration of electrons in the space charge electric field of the ionization wave. The main difference is that classical streamer propagation relies on generation of seed electrons via photoionization [28] while it has been concluded that photoionization is not essential in plasma jets since seed electrons are already present from previous

discharge cycles [3]. However, photoionization may increase the propagation velocity of ionization waves in APPJs. Another major difference with classical streamers is that in free space the propagation path is stochastic while in APPJs the direction of propagation of streamer is pre-determined by the dielectric tube and the noble gas jet axis [3].

2.2.4. The velocity of the ionization wave

In the case of APPJs working in the kHz range the travelling velocities of ionization fronts have been measured to be in the range of 10^4–10^7 m/s [3]. According to a number of studies, velocity of the ionization front is affected by several experimental parameters including electrode geometry [34], gas type [35], excitation voltage amplitude [36], polarity [23, 37] and frequency [38, 39].

A recent study [34] compared the effect of two electrode geometries: a DBD-like configuration (figure 2.1a) and a single ring electrode with a second grounded plate electrode placed 2 cm downstream from the tube orifice (figure 2.1b). It is important to note that in the latter configuration the ionization front reached the grounded plate electrode. A similar accelerating propagation was observed for both configurations but the maximum velocity of the ionization front reached 8 km/s for the DBD-like jet and 40 km/s for the second set-up.

A lot of research on APPJs has been performed in noble gas flows of helium and argon but only recently a comprehensive study was performed comparing the effects of gas type (helium or argon) on the ionization wave velocity [35]. It was shown that with similar APPJ set-up the maximum velocity of the ionization wave is 2–3 times higher in He than in Ar [35].

The voltage amplitude has been shown to increase the ionization wave velocity in several experimental [12, 34] and theoretical works [19]. In a study by Karakas *et al* [36], the velocity increased from 50 km/s to almost 250 km/s when the amplitude of the unipolar positive voltage pulse was increased from 4 to 7 kV. Xiong *et al* [38] showed an increase of the maximum velocity from 150 km/s to 250 km/s when the applied voltage was increased from 7 to 9 kV. Boeuf *et al* [19] have calculated that the maximum velocity increases from 14 to 23 km/s as the applied voltage is increased from 4 to 6 kV and also point out the effect of pre-ionization density on the propagation velocity. Finally, it was observed by Ning *et al* [40] that at higher excitation voltages two consecutive discharge pulses may appear. These two separate ionization waves travel with velocities that differ by two times. The first ionization wave travelled with velocity of 6 km/s while the second ionization wave velocity reached 12 km/s.

Besides the applied voltage amplitude also polarity, frequency and wave-form are known to influence the propagation velocity of ionization waves. It has been shown with calculations [23] and in experiment [37] that both the maximum velocity and propagation distance are lower during the negative half-cycle. It has been proposed that these differences are analogous to positive and negative streamers which were described in section 2.2.2. The increase of

frequency of the applied voltage from 1 to 10 kHz has been shown to influence the temporal evolution of reactive species [38] while the maximum velocity and propagation distance were not influenced. Contrary, in another experimental study [39] the maximum velocity increased from 18 to 33 km/s as the frequency was increased from 2.5 to 20 kV. Different outcomes can be explained by the different electrode geometries: in the first study [38] the powered electrode was inserted in the quartz tube (figure 2.1d) while the second study [39] used a DBD set-up of two ring electrodes around the dielectric capillary (figure 2.1a).

The waveform has been shown to have a strong effect on the ionization wave velocity. Pulsed excitation led to almost two times higher maximum velocity than sinusoidal excitation (24 km/s and 13 km/s, respectively) [41].

Finally, inside a thin capillary the ionization wave velocity has been shown to depend on the dielectric tube diameter [15, 16] but no systematic study on effect of the dielectric tube diameter on the ionization wave velocity in He APPJs has been performed.

2.3. Plasma parameters in non-equilibrium APPJs

2.3.1. The concept of a non-equilibrium plasma

Plasmas are often classified as thermal and non-thermal plasmas [28]. Thermal plasmas can often be classified as thermodynamic equilibrium (TE) or local thermodynamic equilibrium (LTE) plasmas which allows the simplest description of the plasma. Plasma parameters i.e. electron and gas temperature and electron density are relatively easily obtainable by spectroscopic means in the case of thermodynamic equilibrium [42]. TE plasmas are described by one single temperature T, which is the same for all particles and radiation. The distribution of translational energy of plasma particles ε_T is given by the Maxwell energy distribution function with temperature T. The internal energy is distributed among excited electronic, vibrational and rotational levels according to the Boltzmann distribution

$$\frac{n_j}{n_0} = \frac{g_j}{g_0} \exp\left(-\frac{\varepsilon_j}{k_B T}\right), \tag{7}$$

where n_j and n_0 are the concentrations of particles on the level j and ground state and g_j and g_0 their statistical weights respectively. In addition, in the TE plasma the Boltzmann equation also describes the chemical equilibrium, the Saha equation describes the ionization-recombination balance and radiation is in equilibrium with the plasma and is given by the Planck's law for blackbody radiation [28, 42].

LTE assumes one temperature for all plasma species but this temperature varies in space [28, 42]. This temperature can be identified with the spectrally determinable excitation temperature. In addition, LTE model allows for optically thin plasma which means that radiation is not in equilibrium with

plasma. Typically, this is true for atmospheric non-equilibrium plasmas and the intensity I_{pq} which is a measure of radiation power of the transition p→q given by

$$I_{pq} = n_p A_{pq} h\nu_{pq}, \tag{8}$$

where n_p is the population of the upper level, A_{pq} is the Einstein coefficient for the given transition, h is the Planck constant and ν_{pq} is the transition frequency. By registering the intensity of a given transition with a spectrometer the relative population of the upper state of the transition can be determined. By representing the relative populations in the Boltzmann plot [42], the temperature can be obtained according to equation (7).

Non-thermal plasmas typically deviate from the thermodynamic equilibrium which means that the energy distribution of different species can be characterized by different energies and translational and internal energy of plasma species is not in thermodynamic equilibrium [28, 40]. The cause of thermal non-equilibrium is particular to each plasma system but several general physical reasons can be listed. Due to the electron-to-ion mass ratio in the order of 10^{-5} the kinetic energy exchange between electrons and heavy particles is low. In addition, there exist gradients and fluxes of electron densities which cause an energy flux out of the plasma. Furthermore, APPJs produce non-thermal highly non-equilibrium plasmas in short time frames of a few hundred nanoseconds to a few microseconds which is shorter than the typical time required for thermodynamic equilibrium to establish (~ms) [28, 29]. As a result, the electrons and heavy particles (neutrals and ions) have considerably different translational energies which can be characterized by different temperatures. The gas temperature remains below 1000 K (often at room temperature) while electron temperatures can reach 10 000 K.

Partial local thermodynamic equilibrium (PLTE) is sometimes used to describe non-equilibrium systems. It assumes that only part of the population of excited states, electrons or ions is in thermodynamic equilibrium and the energy distribution can be characterized by the temperatures T_{exc}, T_e or T_+ differing for each species [42]. T_{exc} can be again obtained from line intensities according to equation (7) but it is only weakly related to electron temperature [28, 42, 43].

2.3.2. Recombining and ionizing plasmas

In the case when the LTE is not valid and/or in the region of states where PLTE is not applicable the complete balance of excited levels in non-thermal plasmas is given by the Collisional Radiative Model (CRM) [42, 44]. CRM is a set of coupled rate equations for each excited level, for the ground state and for ions under specific plasma conditions [44] which takes into account the total population flux into and out of the level. These equations are solved numerically. The population flux into the level consist of the electron impact excitation from

the lower lying levels, collisional and radiative de-excitation from higher levels and recombination [44]. The population flux out of the level is the sum of collisional de-excitation to lower levels, electron impact excitation to higher and lower levels, electron impact ionization and radiative depopulating [44].

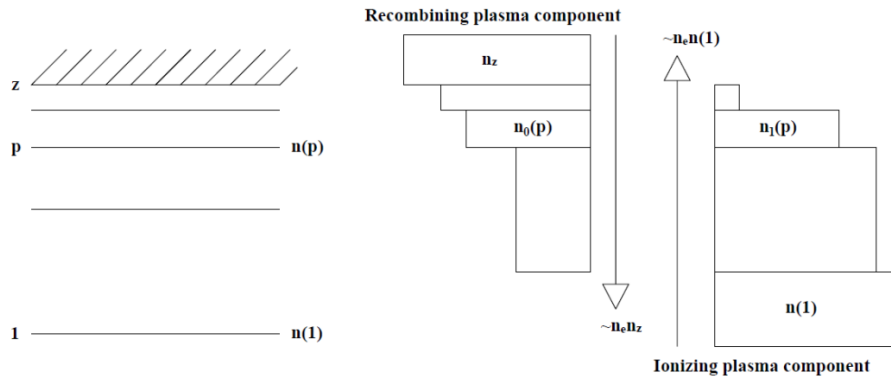

Figure 2.5. Schematic energy level diagram (left) and the concept of ionizing and recombining plasma components (right).

It is possible to isolate contributions from two separate population channels for a specific excited level p with population $n(p)$ for a simplified structure of excited levels as depicted on figure 2.5. The contribution from ions with density n_z is termed recombining component $n_0(p)$ and the contribution from the atomic ground state is termed ionizing plasma component. In general, the ionizing component increases for levels closer to ground state $n(1)$ while recombining component decreases for these levels [44].

The plasma as a whole can be characterized as ionizing or recombining if either of the components is dominant and the plasma is far from ionization balance as a result of time dependence or spatial inhomogeneity. An ionizing plasma is defined as $[n_z/n(1)]<<[\ n_z/n(1)]_{IB}$ with IB denotes the plasma in ionization balance. In this case $n(1)$ is overpopulated. A recombining plasma is defined as $[n_z/n(1)]>>[\ n_z/n(1)]_{IB}$, with n_z being overpopulated [44]. As an important example, the ionizing component may dominate when the charges are removed from the plasma by diffusion and the recombining component is consequently decreased.

It has been shown that APPJs plasmas are ionizing [45] with the majority of atomic state distribution function (ASDF) deviating from the Boltzmann distribution. Only the excited levels closest to the ionization threshold are in equilibrium. The distribution of excited levels detectable from the emission spectrum is characterized by excitation temperatures T_{13} and T_{spec} which are determined by the Boltzmann plot method [42]. T_{13} and T_{spec} characterize the lower and the middle part of the ASDF in He and were found to be ~15 000 K

and ~3000 K, respectively [45]. T_{13} is closer the real electron temperature but requires absolute intensity measurements while T_{spec} is easier to determine but it is only weakly coupled to the electron temperature.

2.3.3. Effect of reducing plasma dimensions

The losses of charged and excited species due to diffusion are an important feature of plasmas and can determine the state of the plasma [28]. Diffusion losses grow as the plasma dimensions or pressure is reduced. On the other hand, it is known that with increasing pressure the electron and gas temperatures tend to equalize and non-equilibrium can be sustained by decreasing the physical size of the plasma [13]. The diffusion losses of electrons and ions to the walls can be expressed by the diffusion frequency ν_D

$$\nu_D = {D_A}/{\Lambda_D^2}, \tag{9}$$

where D_A is the ambipolar diffusion coefficient and Λ_D is the characteristic diffusion length given for cylindrical geometry as

$$\frac{1}{\Lambda_D^2} = (\frac{2.4}{R})^2 + (\frac{\pi}{L})^2, \tag{10}$$

where R and L are the radius and length of the cylinder, respectively [14]. The ambipolar diffusion characterizes the combined diffusion of ions and electrons and can be approximately given for non-equilibrium plasmas as

$$D_A = \frac{\mu_i}{e} \cdot T_e, \tag{11}$$

where μ_i is the mobility of ions which decreases with pressure, T_e is the electron temperature and **e** the elementary charge.

In self-sustaining plasmas operating at stationary steady state the charged particle losses are compensated for by ionization. As the diffusion losses increase with decreasing plasma confinement size the electron temperature must grow to account for the increased losses by enhancing ionization rate $k_i \sim \sqrt{T_e} \cdot \exp(-I/T_e)$, where I is the ionization potential. At the same time the increased diffusion of the heavy particles from plasma to the walls results in more effective cooling and the combined effect is increased non-equilibrium as the plasma dimensions are reduced [14].

2.3.4. Non-equilibrium plasma chemistry

The non-equilibrium plasma chemistry offers selectivity and energy efficiency advantages over thermal plasmas in areas such as pollution control, volatile organic compound (VOC) removal because the input energy into non-thermal plasma is used mainly for the production of energetic electrons in contrast to thermal plasmas where the whole gas stream is heated.

The ozone synthesis which is one of the oldest known plasma chemical processes [46] is a good example of low-temperature atmospheric pressure plasma chemistry. It is based on creation of active species by direct electron impact excitation and further reactions of these excited species [46]. The endothermic synthesis of ozone is a result of a three body collision between O atom and O_2 molecule in non-thermal (near room temperature) dry air plasmas The O radicals are produced in discharge by the dissociation O_2 molecule as a result of electron impact. The gas temperature has to remain close to room temperature to prevent the dissociation of O_3 [46].

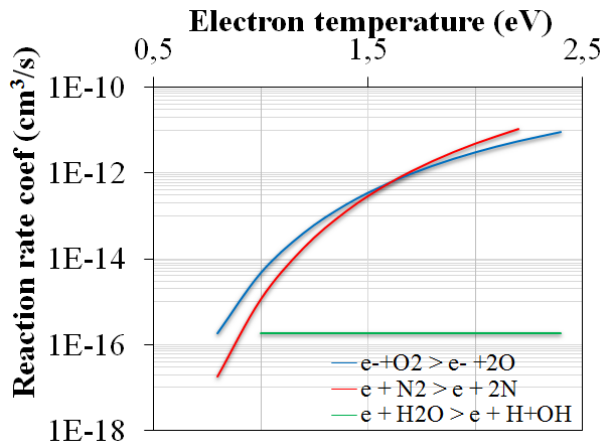

Figure 2.6. Reaction rate coefficient (cm^3/s) as a function of electron temperature for three different reactions in plasma.

The efficiency of non-thermal plasma chemistry is determined by the specific reaction mechanisms and the electron energy distribution function (EEDF). It is primarily the high energy electrons of the distribution "tail" that take part in excitation and ionization. The selectivity of non-thermal plasmas is based on selective excitation of species typically by direct electron impact or through some more complicated pathway. The control over excitation is established by tailoring the EEDF or electron temperature by adjusting the external parameters (e.g. applied voltage). Figure 2.6 illustrates this by showing production rate of three direct electron impact reactions as a function of electron temperature

calculated with data from Niemi *et al* [47] As a rule, the EEDF is non-maxwellian in non-thermal discharges and has to be calculated separately for specific operating conditions.

APPJ research has in large part been motivated by biomedical applications which are based on reactive oxygen species (ROS) and reactive nitrogen species (RNS) chemistry. The production of reactive species responsible for low-temperature plasma chemistry such as reactive oxygen species (ROS) and reactive nitrogen species (RNS) involves several hundred reactions [48]. The RNS originate mostly from nitric oxide (NO) and include nitrogen dioxide (NO_2), nitrate (NO_3) radicals and various non-radical species. The ROS include hydroxyl (OH), hydroperoxyl (HO_2), carbonate (CO^-_3), alkoxyl (RO), super-oxide (O^-_2), carbon dioxide (CO^-_2) etc radicals and several non-radical species such as ozone (O_3), singlet oxygen ($^1O_2$) etc.

The ROS and RNS based plasma chemistry can potentially be improved by reducing the plasma dimensions which ultimately leads to an EEDF with larger "tail" part with high energy electrons. The increased T_e at smaller plasma dimensions can result in increased generation of active species. It has been shown with molecular beam mass spectrometry that a micro-plasma-jet compared to an APPJ in the millimeter range produces higher concentrations of O_3^-, H^+, CO_3^- and O_2^- [22]. The main method for measuring concentrations of species such as OH* radical and O* radical is laser induced fluorescence (LIF) [49-51]. It has also been shown that both the He flow rate and the electrode position relative to each other can affect the temporal evolution of active species concentration [49].

2.4. Applications of APPJs

2.4.1. Biomedical applications

Plasmas have been used as a means for sterilization in packaging, food industry and medicine for some time already [4], but the advent of cold atmospheric plasma sources (CAPs) including APPJs with gas temperatures of less than 40°C has only recently sparked the research for plasma medical applications on living tissues. The interdisciplinary research area involves chemistry, physics, engineering, plasma-engineering, biology, microbiology and medicine. In large part, the research of APPJ has been driven by their applicability for biomedical purposes.

Certain safety regulations apply concerning various aspects of CAPs operation when treating living tissues. Ultraviolet (UV) radiation can cause changes to the DNA and lead to cell death and a maximum rate of allowed UV radiation has been set at 30 $\mu W/cm^{-2}$ [4]. Species with longer life-time, such as O_3, NO and NO_2 can be harmful to living organism in excess amounts and therefore an upper limit or 50 ppb is recommended for O_3, 5 ppm for NO_2 and 25 ppm for NO over a period of 8 hours. As some plasma sources employ the human skin

as a second electrode an upper limit of 0.5 mA at 1 kHz and 20 mA at 100 kHz are set.

Plasma based sterilization effect is historically known for over a century but the application of CAPs dates back only to the end of the 20th century [4]. There are two major areas for application of CAP in sterilization: firstly sterilization of medical equipment primarily in hospitals and secondly sterilization of biological surfaces for example human skin. Both areas expect efficient inactivation of bacteria but while the sterilization of medical equipment poses little safety concerns the biological surfaces require that the treated sample or patient is protected from potentially harmful species in the plasma.

The four main inactivation mechanisms include heat, UV-radiation, charged species and reactive species. Temperature as high as 170°C and UV radiation in range of 200- 300 nm with power density of a few mW*s*cm^{-2} are required to kill bacteria. Gas temperatures in CAPs are close to room temperature and it has been shown that no significant emission occurs below 285 nm with a power density of only 50 μW*s*cm^{-2} [52]. Therefore, charged and reactive species are mainly responsible for antibacterial activity in CAPs. Charged species accumulating on the outer shell of a cell cause an electrostatic force outward from the cell that will result in the cell rupture if it exceeds the tensile strength of the cell. Reactive species such as already described ROS and RNS are able to permeate the cell wall and cause cell death.

The possibility to treat cancer with CAPs has emerged during the past decade with the development and advancement of cold plasma sources [53]. The effect of cold atmospheric plasmas is to induce apoptosis in the cancer cell. Apoptosis is a programmed process which leads to cell death and can be activated intrinsically or externally. The effect of CAPs in treatment of cancer cells has been shown to be twofold [54]. Firstly, ROS are produced in the plasma in contact with the treated sample and the active species are transported into the cell causing cell death. A second possibility is that various radicals and/or RNS play a role in cell signaling pathways. That means that RNS or active radicals [55] created in the plasma enter the cell and make the cell produce extra ROS leading to above threshold levels of ROS for cell apoptosis.

2.4.2. Surface treatment and modification

Low-temperature plasmas at low pressures have been utilized for surface modification, etching, thin film deposition and cleaning of surfaces for several decades in the microelectronic and polymer industry [56]. Atmospheric pressure treatment removes the need for additional vacuum equipment that is often expensive and complicates the treatment process [57]. Temperatures down to room temperature are achievable in atmospheric pressure plasmas including APPJs [2] which allows for treatment of temperature sensitive substrates such as already described biological samples and also industrial polymers. A distinct advantage of APPJs as compared to e.g. DBDs is the possibility to locally treat

3D structures as the plasma is not confined in the narrow region between the electrodes [9]. A further advantages of plasma treatment compared to chemical methods is its environmental friendliness.

Since APPJ device dimensions are in the millimeter range a very small defined treatment region is attainable allowing for precise local treatment. Furthermore, it has been proposed that reducing the physical size of the plasma down to nanometer size can have even more pronounced emergent effects on nanomaterial synthesis [58]. Some interesting published results on plasma synthesis of nanomaterials include carbon nano-spheres created by a plasma in a liquid method [59], growth of graphene at several hundred degrees lower temperature than with chemical methods [60] alumina nanoparticles created in acids [61].

Many industrial polymers such as polyethylene, polypropylene, polystyrene, polyethylenterephthalate have low surface energy which results in poor adhesion and wettability [62]. At the same time the melting temperature of these polymers is a few hundred degrees which necessitates strict temperature control. In several works adhesion improvement due to increased surface energy [62, 63] and decreased contact angle i.e. better wettability [64, 65] have been observed after plasma treatment. In a study [62] PET, PE and PP were studied and the appearance of several oxygen containing functional groups like OH, CO, COH and NOx=1,2 were found after plasma treatment. Plasma treatment has also been employed to several natural polymers most of which are heat sensitive such as plant fibers [66] and various textiles [67] and also to bio-degradable polymers [68].

Plasma enhanced chemical vapor deposition (PECVD) is a well-known method for producing thin films with well controlled morphology and chemistry [69]. In addition to the advantages of atmospheric pressure operation mentioned previously APPJs offer some additional features for the CVD process such as localization of reactor wall pollution caused by low diffusion, deposition in small volumes down to nanoscale, low-volatility liquids can be used as aerosol precursors [69], fast deposition rates and capability to grow patterned and nanostructured surfaces [70]. Furthermore, an important advantage of utilizing APPJs is the possibility to produce thin films locally in small areas (~1mm^2).

3. RESEARCH AGENDA

The main aim of the present study was the investigation of the effect of dielectric tube diameter on various plasma characteristics. It was shown in previous sub-chapters that the plasma characteristics in an APPJ are affected by a number of external parameters and the configuration of the plasma jet. As a consequence, the first part of the work deals with the characterization of an APPJ in a quartz tube with fixed tube diameter of 500 μm. The considered APPJ has a single electrode configuration and is excited by a sinusoidal voltage waveform in the kHz frequency range. The determination of the sensitivity of the electrical characteristics (ignition and sustaining voltage and current pulses), plasma parameters and the propagation of ionization waves on the external parameters (applied voltage, gas flow rate, electrode distance) constitutes the first part of the study.

Second part of the thesis is concerned with the effect of the dielectric tube diameter on:

a) The plasma sustaining voltage.
b) The ionization wave velocity.
c) Several plasma parameters i.e. electron concentration, N_2 rotational temperature and He excitation temperature.

Quartz tubes with inner diameters ranging between 60–500 μm are used in these studies.

Final section of the theses describes preliminary experiments with Yttria stabilized ZrO_2 microtubes which should have 10 times larger dielectric constant when compared to quartz. The goal was to characterize the plasma in Y-ZrO_2 microtubes by spectroscopic means and to determine the ionization wave velocity in an Y-ZrO_2 microtube.

4. EXPERIMENTAL SET-UP AND METHODS

4.1. Experimental set-up

The experimental set-up used in the studies in this thesis is shown in figure 4.1. Spectral characterization and determination of plasma parameters (n_e, T_{rot}, T_{exc}) was performed with only a single electrode (without the ground electrode) and the optical fiber was connected to a spectrometer. The characterization of the 500 µm tube and the determination of ionization wave velocity were performed with the exact set-up shown on figure 4.1 and utilizing a photomultiplier tube (PMT).

Commercially available quartz microtubes with a fixed wall thickness of ≈10 µm and a series of inner diameters D_{in}= 500, 300, 200, 100 and 80 µm and wall thickness of 10±5 µm were used in the experiments. The inner diameter of the tubes was measured with the uncertainty of 20 µm. A photo of a working plasma jet in a 500 µm quartz tube is shown on left side of figure 4.2. The two electrodes, the tube orifice, a glass plate and the He flow direction are highlighted in the figure. The glass plate is used to avoid bridging of the discharge and possible arching.

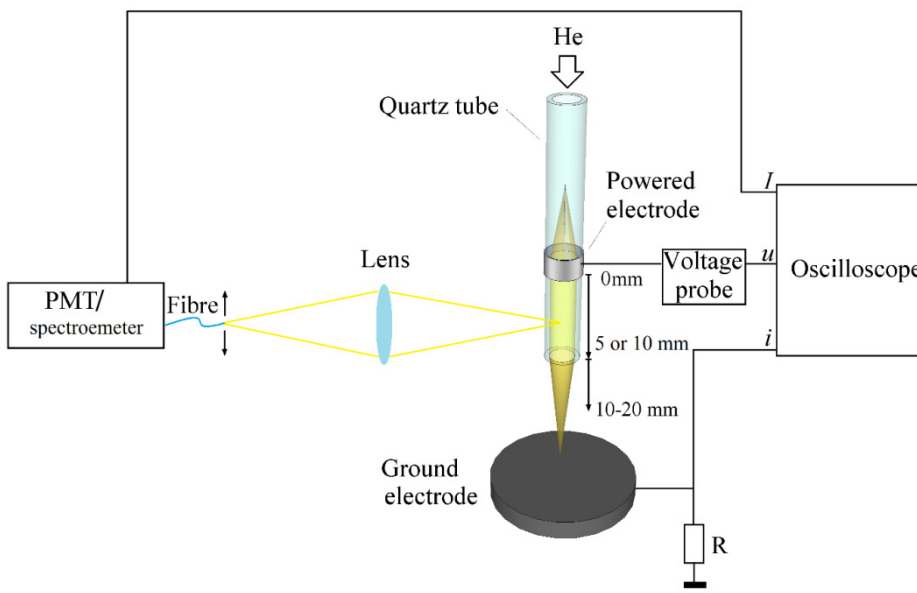

Figure 4.1. Experimental set-up (*R* – resistor, *i* – current, *u* – voltage and *I* – emission intensity measured by photomultiplier PMT or recorded with a spectrometer). Spectral characterization was performed without the ground electrode.

The 1 mm wide powered cylindrical electrode was placed around the tube either 5 or 10 mm from the microtube orifice (figure 4.1). The electrode was prepared by wrapping a 100 µm diameter copper wire 10 turns around the tube. The surface of electrode was smoothened by soldering indium on the wrapped wire and connections to avoid sharp edges of electrode. This electrode allowed to reduce the contribution of discharge outside of the tube [**I**].

The grounded electrode was a copper plate with the diameter of 20 mm and it was placed 20 mm downstream from the tube orifice (figures 4.1 and 4.2), In some tests the grounded electrode was set 10 mm downstream of the tube orifice but the jet was found to be less stable at this condition. The used electrode configuration produced longitudinal electric field along the axis of the tube [**I**].

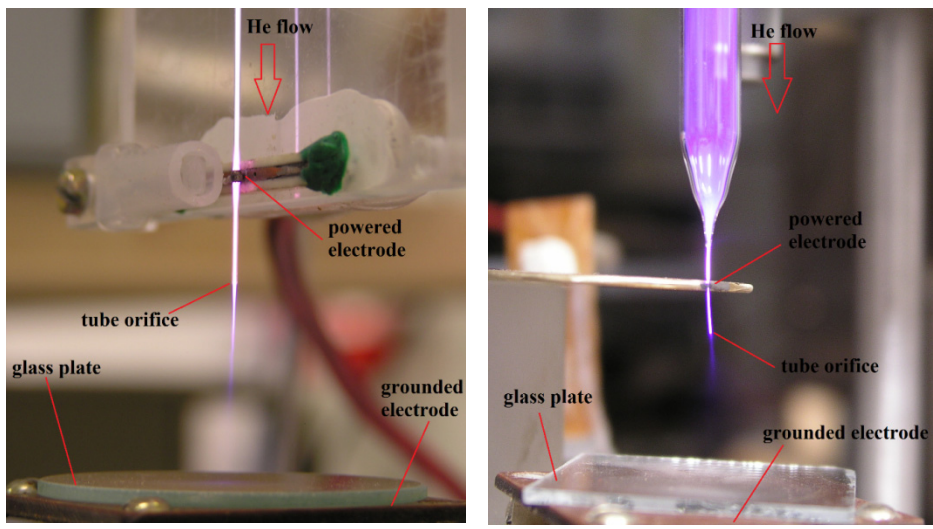

Figure 4.2. Photo of the plasma jet in a 500 µm quartz tube (left) and of Y-ZrO_2 microtube (right).

A photo of a working plasma jet inside Y-ZrO_2 tube is shown on the right side of figure 4.2. The Y-ZrO_2 tube was melted onto a larger silica capillary. The electrode was constructed on the Y-ZrO_2 tube 5 mm from the orifice using platinum paste. It was then mounted on a platform that was movable by micrometer screws in three directions. Sustaining voltage of this Y-ZrO_2 microtube was 16 kV, but we observed that the voltage varies from one tube to another.

Helium with purity of 5.0 (99.999%) was fed into the microtube with the flow rate in range of 10–500 sccm set by an Alicat Scientific flow controller. These flows corresponded to linear velocities of 0.1–200 m/s for different tube diameters. All experiments were carried out in the laminar flow regime [24]. Details of flow rate, linear velocity and Re number are given in table 4.1. In the

experiments concerning the comparison of ionization wave velocity for different tube diameters, the flow rate was adjusted so that the Reynolds number given by equation (1) was Re = 200, which is near the upper limit of laminar flow regime and results in maximum length of the He jet. The estimated pressure inside the tubes with 100 μm diameter (5 mm from the tube orifice) was approximately 170 kPa at 100 sccm.

Table 4.1. Re number, flow rate and linear velocity given for 80, 100, 200, 300 and 500 μm diameters.

diameter (μm)	Re number	flow rate (sccm)	line velocity (m/s)
80	200	80	266
100	200	100	213
200	200	200	106
300	200	300	71
500	200	500	43
500	119	300	25
500	40	100	8
500	8	20	1.7

4.2. Measurement of electrical characteristics and ionization wave development

The sustaining voltage was determined by igniting the discharge at high applied voltages and subsequently decreasing the voltage until the discharge extinguished. For the ionization wave velocity determination, the amplitude of the applied voltage, V_A, was set 1 kV above the sustaining voltage for each tube diameter. Sustaining voltage was determined for each tube diameter at the start of the experiments. At these conditions, a single ionization wave was usually observed during a half-period while at higher voltages multiple ionization waves occurred.

Electrical characteristics were recorded with the Tektronix TDS-540B oscilloscope. The voltage was measured with a capacitive voltage divider and 1:10 Tektronix P6139A probe. In ignition voltage measurements the Velleman PCS-500 oscilloscope was used instead. Current was determined from the voltage drop on the resistor, R. Optical emission from the plasma was collected with an optical lens system with focal length of 60 mm and projected with the magnification of 1:1 onto an optical fiber (1 mm diameter) coupled with the Hamamatsu 1P28A PMT or a spectrometer. The end of the fiber was movable along the projected jet axis with the spatial resolution of 1 mm. Time delays

caused by different lengths of cables and the PMT was taken into account in the figures shown in section 5 and in the calculation of the ionization wave velocity.

The 500 μm tube was characterized more thoroughly. The number of current and emission pulses during one period of applied voltage was determined by recording waveforms of one half-period with high sampling rate and with resolution of 500 ns/div. The oscilloscope trigger was set to 0 V of voltage signal and the optical emission was collected 5 mm downstream from the electrode. Using the same experimental conditions, the procedure was repeated several times to obtain statistically more reliable information.

The development of a certain ionization wave was determined for all tube diameters by recording the electrical current and light emission by the means of PMT signal during single current pulse. For these experiments, the trigger levels were set to select the current signal within certain amplitude range which corresponded to 75–90% of the highest recorded amplitude. The light emission was recorded along the axis of the tube and He jet by moving the optical fiber along the projection of the jet in steps of 1 mm. In these measurements, the resolution was 200 ns/div (2 ns per data point). The propagation velocity of the ionization wave was calculated from the time delay between the onsets of radiation in different positions along the tube axis.

4.3. Spectroscopic measurements

Spectral measurements were carried out in a similar way as ionization wave measurements. In this case a single quartz lens with a focal length f= 75 mm was used. It focused the emitted light with magnification 1 onto the optical fiber of 0.8 mm in diameter. The emission of the plasma jet was collected in 1 mm steps along the tube-length of 5 mm between the electrode and the outlet of the tube (figure 4.1).

Spectra were recorded with two different spectroscopic systems. The spectra in the broad range of 230–850 nm were obtained by Andor Mechelle-5000 spectrometer coupled with an iCCD camera. The spectral resolution of the spectrometer was 0.045 nm at 230 nm and 0.155 nm at 750 nm. This setup was used for the estimation of He excitation temperature. He lines at 447.1, 471.3, 492.2, 501.6, 587.6, 667.8, 706.5 and 728.1 nm were used in these measurements. The MDR-23 spectrometer (grating of 1200 grooves per mm) coupled with the Apogee Alta U1107 CCD camera gave somewhat higher resolution in the spectral region 300–500 nm (FWHM ca 0.06 nm). This setup was used for the recording of the emission from trace impurities N_2 and H which allowed the determination of N_2 rotational spectra and the measurement of the broadening of the H_β 486.1 nm line. Relative spectral sensitivity of both systems was determined in energetic units by using a deuterium-halogen calibration source Ocean Optics DH-2000-Cal.

4.3.1. Electron density

The determination of electron density by Stark effect is based on what is called plasma micro-fields in which all charged particles affect the emitting particle [42, 71]. The majority of spectral investigations of plasma density are based on the hydrogen Balmer series lines H_α (transition 3→2; 656 nm) and H_β (transition 4→2; 486 nm). For these hydrogen lines the Stark effect is linear i.e. the frequency shift of a Stark component changes linearly with the electric field. At atmospheric pressure and low temperatures the Stark broadening of the H_β line becomes dominant above electron concentrations of $5 \cdot 10^{13}$ cm^{-3} [72, 73]. In this work the electron density was determined according to the formula

$$n_e = 10^{16} \cdot (\Delta_{Stark}/0.94666)^{1.49} \text{ cm}^{-3} \qquad (12)$$

found in reference [74].

The actual line width is a combination of natural, Doppler-, pressure-, Stark- and Zeeman broadening mechanism and apparatus function [42, 71]. The natural broadening which is caused by the uncertainty in energy of the involved levels due to their finite lifetime is typically negligible in plasma spectroscopy (~ 10^8 Hz). Doppler broadening arises as a result of the Doppler effect – the frequency of the emitted radiation changes as a result of motion of the emitting particles. For atmospheric pressure low-temperature plasmas, the Doppler broadening is also unimportant. The pressure broadening has Lorentzian shape and as the name suggests is caused by the density of particles surrounding the emitter. It is composed of three mechanisms: Stark, resonance and Van der Waals broadening [42, 71] which all have a Lorentzian form. The apparatus function of spectral instruments determines to what extent the recorded spectrum deviates from that of the true spectrum. In slit instruments the contributions to the apparatus broadening are from the finite width of the slit and diffraction by the focal aperture. The experimentally measured spectrum is generally a Voigt profile which is a convolution of the Lorentz and Gauss profiles.

The fitting procedure of H_β line for the estimation of electron density is described in article **I**. The main source of error in the determination of electron density was the uncertainty of the fitting by Voigt profile which was between 0.02-0.03 nm depending on the intensity of the line. The broadening due to van der Waals effect was also important and it was subtracted from the total Lorenzian FWHM. The n_e in the units of cm^{-3} was then calculated from Δ_{Stark} according to equation (12).

4.3.2. Gas temperature

The N_2 (C-B, 0-0) transition with the band head at 337.1 nm and N_2 (C-B, 0-2) transition with the band head at 380.5 nm were used to determine the rotational temperature of N_2. The rotational temperature can be determined either from a Boltzmann plot for rotational levels or comparison with synthetic spectra. In present study, the measured spectra were fitted with calculated synthetic spectra in 10 K steps and the temperature assuring the best fit was taken as the rotational temperature [**I**]. Uncertainty of the fitting procedure was estimated from the difference between the temperature allowing best fit and the temperatures where the synthetic and measured spectra started to clearly deviate from each other. The estimated uncertainty was 50–100 K depending on the intensity of emission. The spectra obtained for the N_2 (C-B, 0-0) transition with the band head at 337.1 nm was not used routinely because it had additional features at 336 nm corresponding to NH impurities and this also decreased the accuracy of fitting. However, we checked that the rotational temperatures obtained from two transitions coincided in the limits of uncertainty.

The rotational temperature can be used as a measure of the gas temperature with the assumptions that the rotational quantum is conserved during electron impact excitation from the ground state and the ground state is populated via collisions with heavy particles. Additional possibility is the fast thermalization of rotational distribution of excited states before emission occurs. In the latter case, the excitation of N_2 may also occur by energy transfer from excited heavy particles e.g. He metastables. For He plasma jets, it is usually assumed that these conditions are fulfilled.

4.3.3. Estimation of electric field

It has been proposed that for an atmospheric pressure discharge it is possible to determine the electric field from the intensity ratio of He singlet lines at 667.8 nm ($3^1D \rightarrow 2^1P$) and at 728.1 nm ($3^1S \rightarrow 2^1P$) [75, 76]. The singlet lines were chosen because they are primarily excited from the ground state. The upper level concentration n_p in equation (7) is dependent on the excitation rate which is in most cases a direct function of the reduced electric field. The excitation rate dependence on electron concentration is eliminated by the ratio of the two lines. This is a relative method and requires calibration for absolute electric field measurement e.g. with Stark polarization effect. The electric field is then determined by the change of distance between the He 492 nm line ($4^1D \rightarrow 2^1P$) and its forbidden counterpart ($4^1F \rightarrow 2^1F$). This method was utilized to verify the validity and to calibrate the line intensity ratio method [75]. In the present study, the line ratios were outside of the available calibration range and the line ratios were used only as an indication of electric field values.

5. RESULTS AND DISCUSSION

5.1. Investigation of the APPJ in a 500 µm quartz tube

5.1.1. Effect of applied voltage

For all tube diameters during each period of applied voltage there appeared one or several short (~100 ns) current pulses accompanied by optical emission. Each of these pulses corresponds to the propagation of an ionization wave described in section 2.2.3 and further discussed in section 5.1.3. The time variation of the appearance of the pulse(s) during each half-period (e.g. as depicted on figure 5.1 left) is known as jitter. In our experiments jitter was in the range of a few microseconds. The one possible cause of jitter could be that some of the avalanches do not transition to ionization waves but sink to the walls of the dielectric tube.

Figure 5.1 depicts the current and optical emission registered during one period of the applied voltage at the gas flow rate of F_r = 100 sccm. At 7 kV amplitude voltage only one pulse was detectable during the positive half-period of the applied voltage (figure 5.1 left). With the increase of the V_A to 7.5 kV a second pulse started to appear occasionally and with further increase of the voltage amplitude there was a growing number of half-periods where two pulses occurred. At even higher voltages larger number of pulses started to appear and at V_A = 20 kV up to 7 pulses could be counted during the same positive half-period (figure 5.1 right) and article **II**. During the negative half-period there were two pulses observable already at lowest voltages.

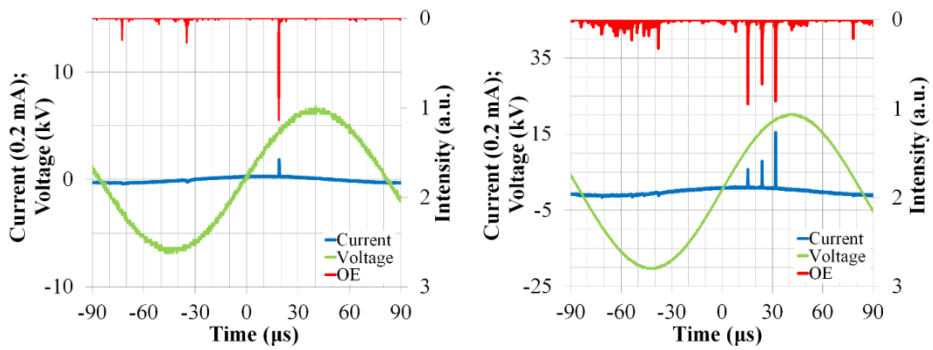

Figure 5.1. Applied voltage waveform and observed current and optical emission (OE) pulses at F_r = 100 sccm at V_A = 7 kV (left) and V_A = 20.5 kV (right). Optical emission was registered 5 mm downstream of the high-voltage electrode.

The number of pulses occurring during the both polarities was investigated more thoroughly by counting the pulses over six half-cycles. The average number of pulses per period during the positive half-period is shown on figure

5.2 as a function of applied voltage for flow rate F_r = 100 sccm. While the flow rate effect on the number of pulses was negligible at lower applied voltages there occurs on average 2 more pulses at 20 sccm than at 500 sccm at 20 kV applied voltage [**II**]. As a conclusion, the main effect of increased applied voltage is to increase the number of pulses per half-cycle.

On average there appeared 1–2 pulses more during the negative half-cycle and a change to what seemed to be a continuous discharge occurred at higher voltage amplitudes (typically at 20 kV) [**II**]. It was not possible to clarify whether the plasma became continuous or the subsequently following pulses were not resolved (figure 5.1 right).

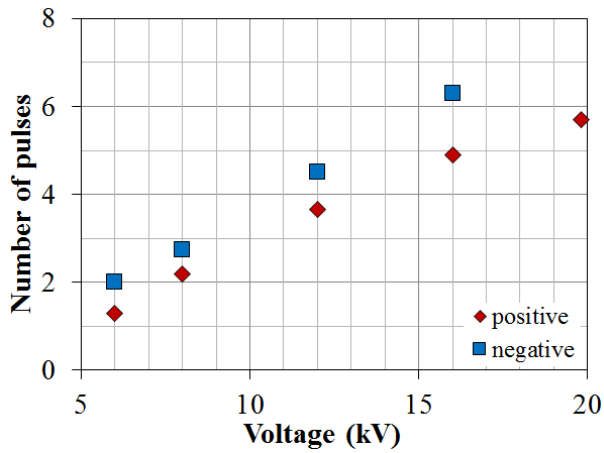

Figure 5.2. Number of pulses as a function of applied voltage amplitude during positive (red diamonds) and negative (blue squares) half-periods.

5.1.2. Effect of gas flow rate

5.1.2.1. Length of the plasma jet

The length of the plasma jet outside of the tube was obtained from the photographs (figure 5.3). There was a transition of the color from white to violet which was attributed to the transition from the emission of He plasma jet to the afterglow of various nitrogen bands. The length of the jet was taken as the distance between the tube orifice and transition point. The length of the plasma jet was mostly influenced by the flow rate (figure 5.3) similarly to the observations of other studies [3, 12]. With the increasing flow rate, the length of the plasma jet reached approximately 2–11 mm depending on the flow rate and tube diameter. The increase of the jet length with increasing flow rate is typically explained by the increased length of the He gas jet that allows ionization waves to travel further [3]. At highest flow rates (above 1500 sccm) the length started to decrease which can be explained by the transition of the flow from the

laminar to turbulent regime [24]. In several other studies [3, 12] the plasma jet length was also influenced by the applied voltage while in our experiments the effect of voltage was too small to be observable.

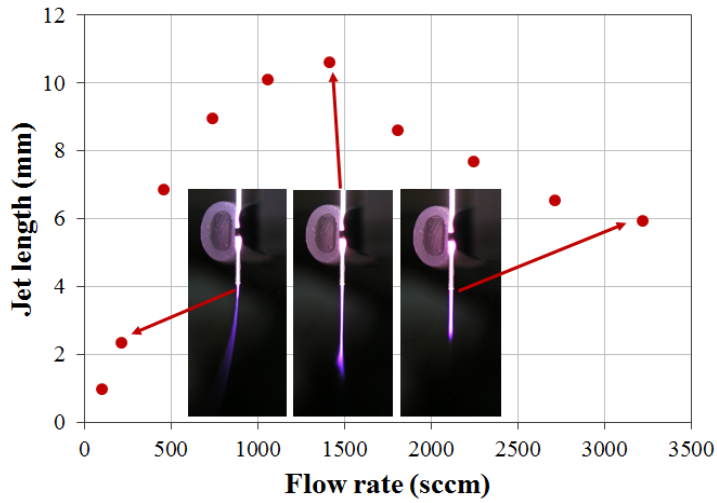

Figure 5.3. The length of the plasma jet as a function of flow rate in a 500 µm quartz tube at V_A = 20 kV. The images of the jet at selected flow rates are also shown.

In subsequent experiments, the flow rates were chosen to cover as wide range of the jet lengths as possible without transition to turbulent regime. The upper limit of used flow rate was 500 sccm which resulted in the Reynolds number of Re = 200 and was clearly in the laminar gas flow regime [24]. Flow rates resulting in the same Reynolds number were later used in the experiments with other tube diameters.

5.1.2.2. Sustaining voltage

When the tube radius was reduced down to 300 µm (sections 5.2 and 5.3) the ignition voltage was above the limit for the power source and ignition proceeded via a Tesla coil. For clarity, therefore throughout this thesis the sustaining voltage is analyzed instead of the ignition voltage. Figure 5.4 shows the sustaining voltage for the 500 µm tube as a function of the flow rate. The sustaining voltage remained similar between 100 to 500 sccm for two electrodes but was somewhat higher for the single electrode configuration (without the grounded copper plate) at 100 sccm. A noticeable increase of sustaining voltage was observed at flow rate of 20 sccm with 500 µm tube and also with smaller tubes. The sustaining voltage was affected by the tube diameter to be described in section 5.3. The sustaining voltage also increased when the electrode sepa-

ration was increased from 2 cm to 3 cm. This is explainable by the decreased Laplacian electric field at the same applied voltage.

At applied voltage V_A values up to 2 kV above the sustaining voltage it was possible to observe single pulses during the positive half-period of voltage for all gas flow rates (figure 5.4). The effect of increasing flow rate was to decrease the voltage at which two pulses appeared similarly as the sustaining voltage was decreased.

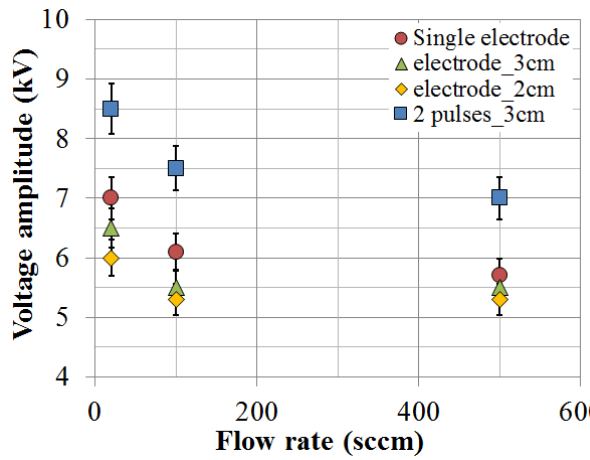

Figure 5.4. The sustaining voltage for the 500 µm tube as a function of flow rate F_r for single electrode configuration and with grounded plane electrode positioned 3 cm (green) and 2 cm (yellow) from the powered electrode. Also shown is the minimum applied voltage amplitude at which at least 2 pulses were detected (blue).

5.1.2.3. Current pulse

The effect of flow rate was further clarified by registering the instantaneous values of electrical current and optical emission with better temporal resolution. At a fixed voltage amplitude and flow rate, the peak values of currents varied in a large range as shown in figure 5.5. For the comparison of the current pulses obtained at different experimental conditions, the trigger levels chosen to record only current pulses with a narrow range of peak values. As an example, for 100 measurements 79% of the current peak values were in the range of 0.1– 0.5 mA for F_r = 100 sccm and V_A = 7 kV as illustrated in figure 5.5. The trigger levels were set at 90% of the highest values observed during these 100 recordings and as an example the trigger was set to record pulses with amplitudes between 0.5–0.6 mA for flow rate of 100 sccm.

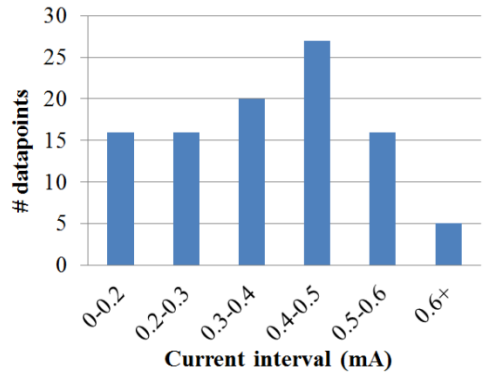

Figure 5.5. Histogram for the current amplitude intervals of 100 measurements at a flow rate F_R= 100 sccm and applied voltage V_A= 7 kV.

The recorded current pulses are shown on figure 5.6. It was confirmed that the shape of the first current pulse of a half-period was essentially the same when voltage amplitudes were higher and had good reproducibility. The full width at half maximum (FWHM) was in the range of 100–500 ns and increased with increasing flow rate. The initial slow increase of the current was similar to all flow rates. With increasing flow rate, the currents continued to rise for longer time which resulted in higher peak values and longer pulse. The average peak values and the FWHM of the pulses increased at least 4 times when flow rate increases from 20 sccm to 500 sccm. After reaching the maximum value, the current started to slowly decrease. Similar trends for current pulses corresponding to first ionization wave were observed for negative voltage polarity at different flow rates.

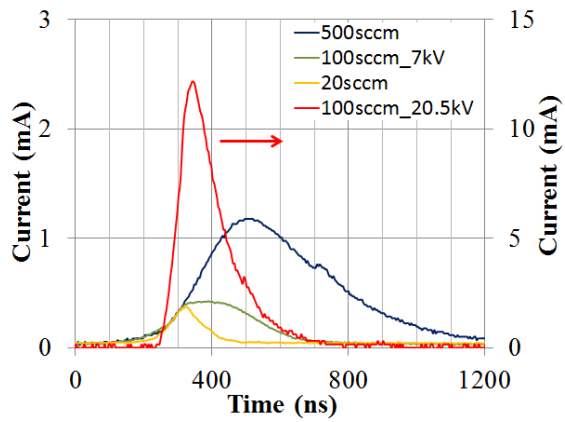

Figure 5.6. Current pulses during the positive half-period with V_A = 7 kV for F_r = 20, 100 and 500 sccm. Current pulse for a subsequent ionization wave (marked with an arrow) is shown on the secondary axis for F_r = 100 sccm.

The shape of a subsequent current pulse of the same positive half-period had much shorter rise time and the maximum observed current value was above 10 mA. The difference in shape between first and subsequent pulses during negative half-period was not as clear as during the positive half-cycle. The initial increase of the currents followed the same trend and also the peak value and FWHM of the pulses increased with increasing flow rate.

5.1.3. Ionization wave propagation

5.1.3.1. First ionization wave of each half-period

The propagation of the first ionization wave of each half-period is shown on figure 5.7 for F_r = 100 sccm. The current pulse (black) is shown together with optical emission pulses registered in several positions along the dielectric tube and plasma jet axis. Positions 3–9 mm are inside of the quartz tube while positions 10–14 mm are outside in the He jet. Similar development was seen for all flow rates and for varying distance (3 cm and 2 cm) of the grounded plate electrode.

Figure 5.7 shows the ionization wave propagation during both the positive (left) and negative (right) half-cycles for V_A = 7kV. At these conditions only one ionization wave per half-cycle is observed (figure 5.1 left) and a more detailed description of the propagation can be found in article **II**. It was not possible to determine the ionization wave development during the first 2–3 mm below the powered electrode as the optical emission pulse had a long onset period of about 300 ns and the signal remained close to the noise level. At 3–4 mm downstream from the powered electrode the emission pulse obtained a clear wave-front with a sharp well-defined onset.

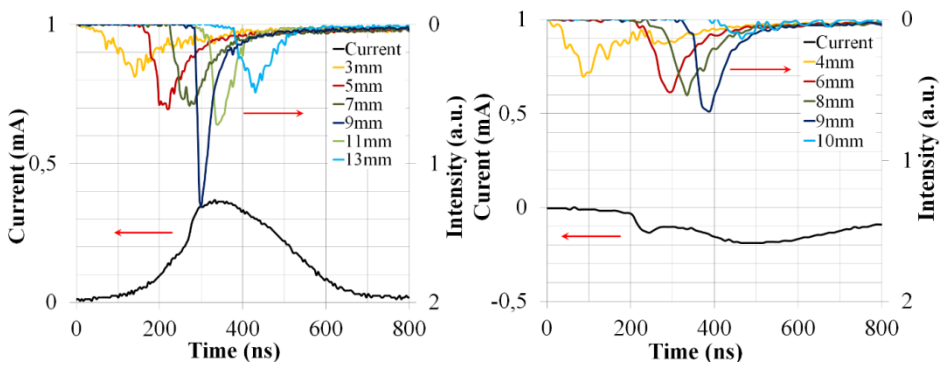

Figure 5.7. Current and optical emission pulses recorded during the positive (left) and negative (right) half-cycle at different axial positions (V_A = 7 kV and F_r = 100 sccm).

Abrupt increase of the emission intensity near the tube orifice was accompanied with the strong increase of emission intensity of second positive system of N_2 molecules and can be explained with the diffusion of ambient air into the He jet. The farthest distance where the emission could be registered increased with the flow rate (≈11, 14 mm and 18 mm for 20, 100 and 500 sccm respectively). The farthest distance where the emission could be registered was in correlation with the length of the plasma jet as shown in figure 5.3.

During the negative half-cycle the emission first appeared at 3–4 mm downstream from the electrode and the ionization wave moved initially towards the powered electrode. A similar phenomenon has recently been observed during few first nanoseconds of the negative corona discharge in air at atmospheric pressure [77]. A clear downstream development of the ionization wave was observed only after the first ionization wave had reached the electrode (figure 5.7). This event can be correlated with a hump in the current pulse at 250 ns in figure 5.7. The optical emission intensity of the ionization wave moving towards the tube orifice increased slightly and reached a maximum at the tube orifice similarly with positive half-period.

In the case of first current pulses of both positive and negative half-periods, the instantaneous displacement current increased as long as the ionization wave moved downstream from the electrode. The increase of the current during the propagation of ionization wave can be explained both by increased velocity of the ionization wave and by the decreasing distance between the ionization front and grounded electrode. The distance covered by ionization wave increased with the flow rate and we consider this as the main reason for increased current pulses at higher flow rates. The results also suggest that the grounded electrode did not influence the development of ionization wave at these conditions and the measured current was displacement current.

5.1.3.2. Subsequent ionization wave of a half-period

Figure 5.8 shows the propagation of a subsequent ionization wave of the positive half-cycle at V_A = 20.5 kV during the positive half-cycle (note the different time-scales as compared to figure 5.7 and 5.8). The emission actually appeared first at the tube orifice (position 9 mm shown in dark blue on figure 5.8) and moved simultaneously towards the powered electrode and downstream of the jet in ambient air. In addition, differently from the first pulse the optical emission intensity was lowest at the tube orifice and increased as the ionization wave travelled in both directions. It can also be seen on figure 5.8 that the emission in the He jet has first a very narrow maximum and then approximately 100 ns later a second broader maximum.

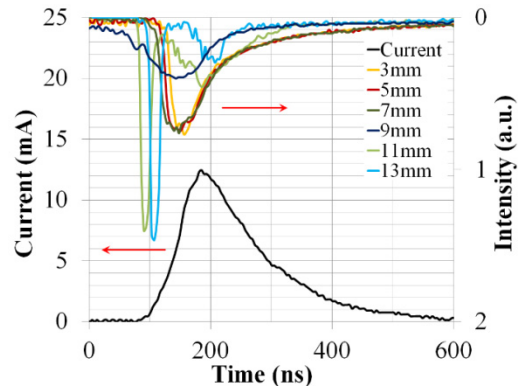

Figure 5.8. Current and optical emission pulses during the positive half-cycle for a subsequent ionization wave recorded at different axial positions (V_A = 20.5 kV and F_r = 100 sccm).

The different propagation behavior of first and subsequent pulses is further illustrated on figure 5.9. The different behavior of the subsequent pulses is explained in detail in article **II**. According to the model proposed there, the surface charge accumulated on the wall during the development of the first ionization wave and reduced the Laplacian electric field inside the tube. The enhanced electric field near the tube opening [25] facilitates the following breakdowns of a same half-period near the tube exit. We found that the time delays between two consecutive pulses remained nearly equal which suggests that the electric field became sufficiently large for the next breakdown after a certain time interval. Similarity with the Trichel pulses of negative corona [78] suggests the possible effect of space charges that accumulated during the streamer development.

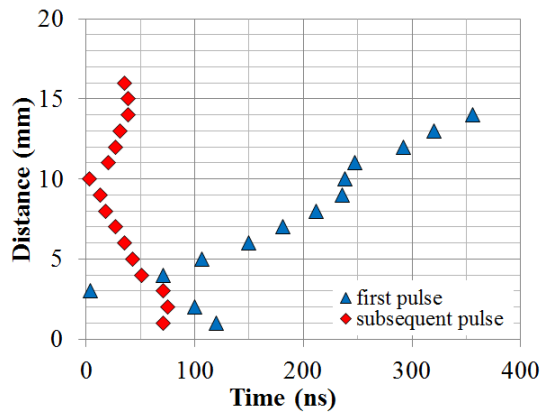

Figure 5.9. The axial distance plotted as a function of time for first and subsequent ionization waves for at F_r = 100 sccm and V_A = 6; 20.5 kV.

5.2. The effect of dielectric tube diameter on the ionization wave velocity

5.2.1. First ionization wave of positive- and negative half-periods

Figure 5.10 depicts the temporal evolution of the ionization front during both the positive and negative half-periods at Re = 200, $V_A - V_{sust}$ = 1 kV for microtube diameters D = 80, 160, 300 and 500 µm. Increase of the applied voltage by several kV had practically no effect on the temporal evolution of the ionization front contrary to the typical observations for pulsed DC voltage (section 2.2.4). Similarly to the results obtained with 500 µm tube, during the first few millimetres the onset of optical emission was not well defined and starting point of the ionization front propagation was taken when a clear steep onset of optical emission was observed (e.g. position 3 mm on figure 5.7). During the positive half-cycles the ionization front can be seen to accelerate during its propagation inside the microtube for all tube diameters (figure 5.10) and the data points were fitted with an exponential function. Outside of the microtube a linear fit was used.

The temporal evolution of the ionization front during the negative half-period was similar to the positive half-period. A notable difference was the suitability of a simple linear fit for the approximation of the data both inside and outside of the microtube.

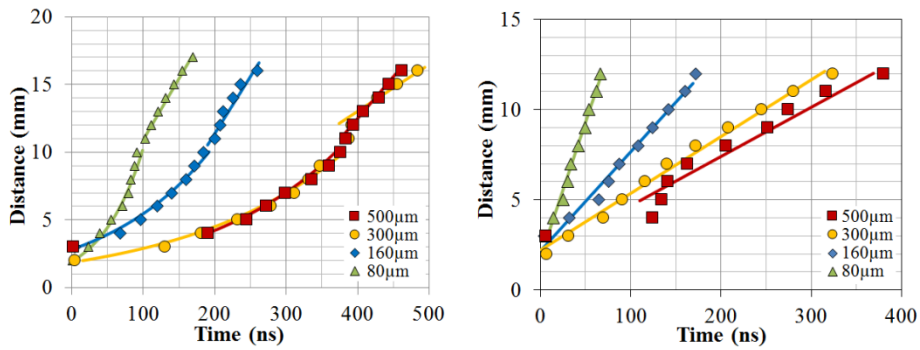

Figure 5.10. Temporal evolution of the ionization wave during the positive (left) and negative (right) half-period. Lines show an empirical fit to the data.

The comparison of the velocity of the ionization front for positive and negative half-periods at the tube orifice is shown as a function of microtube diameter on figure 5.11. There was a clear increase of the velocity as the diameter decreased while the velocity was somewhat smaller for negative half period. However, for positive half-period, the velocity depended also on the position in the tube and it was about two times smaller at the distance of 4 mm from the tube [**III**]. The

largest velocities were 170 km/s and 145 km/s for positive and negative half-periods respectively observed for the 80 µm tube.

The effect of dielectric tube diameter on ionization wave velocity has previously only been observed in APPJ in air by Jansky *et al* [16]. They measured the ionization front velocity inside a microtube (diameter 37.5–300 µm) which was initiated by a pulsed DC voltage and observed increase of the velocity from 200 to 800 km/s when the diameter decreased from 300 µm to 100 µm. The measured velocity values of up to 170 km/s for the 80 µm diameter in this work are an order of magnitude smaller than the aforementioned values in air. This can be explained by stronger electric fields necessary to sustain the discharge in air [19].

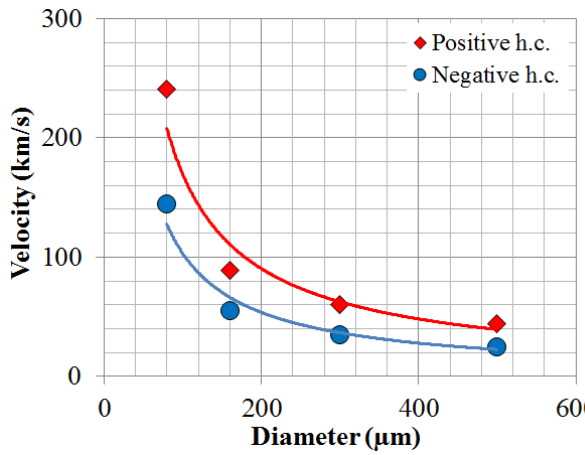

Figure 5.11. Ionization wave velocity dependence on the quartz tube diameter during both voltage polarities. Lines are a guide for the eye.

In He plasma jets, the ionization wave velocities have been measured only for larger tube diameters (typically D~ 2–5 mm) and are in the range of 5–50 km/s [3], however no systematic study has been carried out concerning diameter. The measured velocities are lower for parallel field geometry [21] and for sinusoidal excitation [75] ranging only to about 5–20 km/s. In a plasma jet excited with sinusoidal voltage utilizing similar electrode configuration as in the present study but in a larger quartz tube ((D= 2 mm) velocity has been measured to range from 5 to 40 km/s in the He jet [34]. These velocity values are comparable to what we measured in the case of 300 and 500 µm tubes. Velocity during the negative half-period has been measured to be somewhat smaller than during the positive half-period [3].

In experiments with all tube diameters the maximum velocity was observed at the tube orifice. The increase of the velocity at the tube orifice has been explained by the enhanced electric field at the orifice due to the discontinuity of surface charges [25]. An additional explanation for the continuous increase of

the velocity of ionization wave of positive half-period during the propagation inside of the dielectric tube is the formation of well-conducting channel. According to the ideally conducting streamer channel model described in the section 2.2.2., the electric field in the positive streamer head should increase continuously with channel length. The channel conductivity expectably decreases outside of the tube due to the electron attachment to oxygen molecules.

5.2.2. Possible cause of velocity increase

It has been shown [34, 79], that the velocity of ionization wave is in correlation with the local electric field strength in the head of ionization wave [34, 79] which is the sum of the Laplacian electric field, the electric field of the space charge in the head of ionization wave and the electric field of the surface charge [**III**]. The increase of Laplacian electric field with decreasing tube diameter is connected with the increase of sustaining voltage as shown in subsequent section 5.3. The effect was also obtained by numerical calculations in [26].

The increase of space charge electric field at decreasing tube diameter is not clear. The electron density in the plasma increased from $\sim 10^{14}$ cm^{-3} at 500 μm to $\sim 10^{15}$ cm^{-3} at 80 μm diameter as discussed in section 5.4.2. Furthermore, the calculations of a theoretical study [19] suggested that the electric field on the axis increases with the decrease of tube diameter and the electron density scales as $n_e \sim (1/D^2)$ in the diameter range of 1 to 3 mm. A fit to the data is given on figure 5.14 as $n_e \sim (1/D)$. With the assumption that the thickness of the space charge layer does not depend on the tube diameter, the volume of the space charge scales as $(1/D^2)$. As a consequence, the expected total space charge in the ionization wave remains same or decreases with decreasing diameter.

The electric field of surface charges remaining on the surface from the previous half-cycle is also unknown. It has been shown that the surface charges inside the capillary originating from the previous half-cycle increased the ionization wave velocity in air [80]. A numerical study suggested that the velocity increases with the increase of linear surface charge density [16]. A study by same authors showed [81] that at the same applied voltage, the decrease of the tube diameter from 250 to 100 μm resulted in about two-fold increase of the surface charge density while the surface charge per unit length of the tube remained similar. In our case it is not clear whether the surface charge per unit length remains the same because the potential during breakdown also expectedly increases with decreasing diameter.

5.3. The effect of dielectric tube diameter on the plasma sustaining voltage

As briefly described in section 5.1.2 when the tube diameter was below 300 µm, the ignition voltages were above the available limit of voltage source and proceeded only via external ignition with a Tesla coil. The registered sustaining voltages, V_{Sust}, were somewhat lower than the ignition voltages, V_I; the difference between these two voltages became larger as the tube diameter decreased. The voltage necessary for sustaining the plasma after the first ignition can be smaller due to the surface charges deposited on the dielectric tube during the previous half-cycle as indicated by the presence of current and optical emission pulses already at 0 V (figure 5.1). In addition, the production of residual long lifetime species (e.g. metastables) stores the energy which allows to use lower voltages for following breakdowns. Due to the difficulties with ignition, only sustaining voltage was investigated more thoroughly.

The dependence of sustaining voltage on the tube diameter at the flow rate of 100 sccm is shown in figure 5.12 for the single electrode configuration and for the configuration with two electrodes with the distance of 3 cm. The sustaining voltage increased monotonically with decreasing tube diameter for both configurations. A noticeable difference (2 kV) in sustaining voltage between the two configurations is seen only with the smallest tube diameters of 80 µm. A series of experiments were carried out with the tube of 300 µm diameter by varying the position of the electrode from 2 to 10 mm of the tube edge and the position of electrode had insignificant influence on the sustaining voltage. There was a slight decrease of V_{Sust} at increasing flow rates but the effect of tube diameter was considerably larger when the flow rate was above 10 sccm.

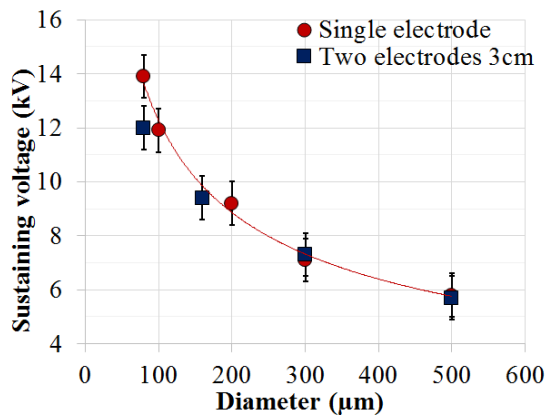

Figure 5.12. Sustaining voltage, V_{Sust}, as a function of tube diameter at a flow rate of 100 sccm (red solid line for the single electrode configuration is a guide for the eye).

The plasma jet configuration with one ring electrode outside the tube studied in this thesis has strongly inhomogeneous Laplacian electric fields which are directed mostly along the tube axis [**I**]. In addition, experimental data shows that the second grounded electrode has little to no influence on the breakdown (figure 5.12). Furthermore, it was verified and can also be seen on figure 4.1 that the gap between the electrodes is not visibly bridged even at highest flow rates which means that the propagating ionization wave does not reach the grounded bottom electrode. These observations suggest that Spark breakdown mechanism as described in sections 2.2 is valid in the present configuration.

One possible explanation for the increase of sustaining voltage at smaller tube diameters is the increased loss of electrons during the development of avalanche. According to the Meek criterion (5), the avalanches transform to a streamer when the electric field of the avalanche space charge becomes comparable to the Laplacian electric field. As shown in Table 5.1, the characteristic diffusion times to the walls calculated according to equations (8-10) become comparable to avalanche development times which are several nanoseconds [82, 83]. As a result of the increased electron losses, it is necessary to increase the ionization rate by applying higher voltage to facilitate the streamer formation as the tube diameter is reduced. Similarly, it has been observed for air plasma inside ceramic foams that the onset voltage of plasma formation increases by several kilovolts as the pore size is reduced from 120 to 70 μm [84].

Table 5.1. Characteristic times of diffusion to the walls for electrons, τ_e, and He metastables, $\tau_{He\,m}$, at varying tube diameter obtained as a reciprocal of diffusion frequency $D/(R/2.4)^2$.

Diameter, μm	τ_e, ns	$\tau_{He\,m}$, μs
100	16	7.8
200	66	31
300	150	70
500	400	200

Furthermore, it was recently shown by calculations of Cheng *et al* [26] that as the dielectric tube diameter is reduced from 1 mm to 0.2 mm the electron concentration prior to breakdown was reduced by almost four order of magnitudes. They argued that this reduction is caused by radial electron drift. Another possible explanation for the decreased pre-ionization level of electron concentration may be connected with the production of electrons via the Penning effect [85]. The time periods before the breakdowns at each half-cycles are between one quarter and one half of the period of applied voltage e.g. between 40-80 μs (figure 5.1). The decrease of tube diameter increases the diffusion losses of He metastables as shown in table 5.1 and the diffusion time

of metastables decreased below 40 µs at tube diameters of 200 µm. Therefore, the density of He metastables and consequently the pre-ionization level can be considerably lower at smaller tube diameters. As a note the He metastable concentration is most probably not affected by depletion by convective the gas flow as argued in article **I**.

5.4. The effect of dielectric tube diameter on electron concentration, N_2 rotational and He excitation temperature

5.4.1. The spectra

The time-averaged spectra of plasma in a 200 µm diameter tube under a flow rate of 100 sccm are shown in figure 5.13. The most intensive bands recorded in the spectral region 300–450 nm belong to trace gases- OH(A-X), N_2(C-B) and various N_2^+(B-X) transitions. Lines corresponding to α and ß transitions of hydrogen Balmer series are also detectable. In the range of 450 to 800 nm there are various He lines (most notably 501.6, 587.6, 667.8, 706.5 and 728.1 nm) and a line belonging atomic oxygen triplet state (777 nm).

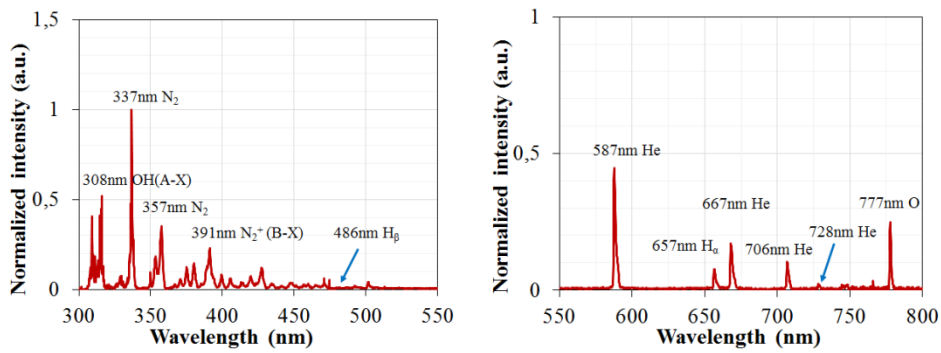

Figure 5.13. Emission spectrum recorded at *3* mm below the electrode for a 60 µm tube and F_R= 20 sccm and V_A= 13.6 kV at two wavelength regions.

He based plasma jets are usually considered to be optically thin [3], i.e. the absorption of the emitted light by the plasma itself is negligible and this was also confirmed for our case. In the case of the tubes with larger diameter, the intensities of the lines varied along the tube as shown in article **I**. At about 3 mm downstream from the electrode the intensity became practically constant up to the tube orifice. Roughly 3 mm below the powered electrode the glow inside the tube somewhat contracted compared to the first few millimeters. This effect has been seen in a recent computational study and it was correlated to the

spatial distribution of electron density in the ionized channel left by the propagating ionization wave [86]. Most of the spectral measurements that will be described below were carried out 3 mm downstream of the electrode to minimize the intensity variation.

The spectra were acquired averaging over large number of applied voltages which makes the interpretation of the following results for n_e, T_{rot} and T_{exc} somewhat difficult because the plasma is formed from the ionization waves as described in section 2.2.3. The propagation timescale of one ionization wave is of the order of a few hundred nanoseconds while the average time delay between the ionization waves is more than 10 µs. The excitation of emitting species occurs mainly during the short time-period (in the order of tens of nanoseconds) when ionization wave passes the discharge volume where the emission is collected [3, 31]. The intensities of registered He lines are expectedly related to the strong electric fields in the head of the ionization wave.

5.4.2. Electron density

Electron concentration was determined for the single electrode configuration from the broadening of Balmer β transition (4-2) of atomic hydrogen at 486.1 nm as described in the section of experimental methods (section 4.3.1). At atmospheric pressures and at low temperatures, the broadening of H_β line is dominated by the Stark broadening, when the n_e is above $5 \cdot 10^{13}$ cm^{-3}[74, 75, 87].

The electron density, n_e, is highest in the formed plasma plume [15, 16, 88] whereas the emission of excited species takes place in the time scale of ≈100 ns ($A_{ij} = 9.6 \cdot 10^6$ s^{-1}) [33] and thus the Stark broadening of hydrogen 486.1 nm line describes most likely the electron density in the discharge channel behind the head of the ionization wave.

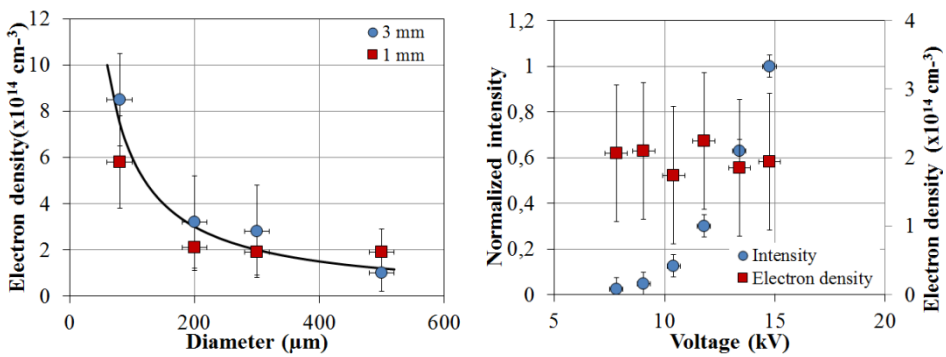

Figure 5.14. Time averaged electron concentration as a function of tube diameter at 15 kV applied voltage for distances of 1 and 3 mm below the electrode (left). The line (1/*D*) is a guide for the eye. Time averaged normalized intensity and electron concentration as a function of applied voltage for 500 µm tube (right).

Electron densities were determined for all tube diameters along the whole tube length downstream from the electrode and at different applied voltages (8–15 kV). The electron densities as a function of diameter obtained at 1 and 3 mm downstream from electrode are shown in figure 5.14 (left). The determined electron density was considerably larger only for 100 μm tube. In the limits of uncertainty, the electron densities remained unchanged in the whole length of the tube while the intensity of H_β line decreased in the direction of tube outlet.

The increase of applied voltage from 8 to 15 kV had no considerable effect on the electron density (figure 5.14) even though the intensity of H_β 486.1 nm line increased more than an order of magnitude. This is consistent with the variation of the number of pulses with applied voltage described in section 5.1.1. (figure 5.1). As the voltage is increased more pulses appear each half-period and the total time-averaged intensity (the sum of intensity of all pulses) increases while the averaged electron density in a single pulse remains similar.

The n_e values determined in the plasma jet with similar configuration as our jet outside of the tube were in the same order of magnitude as what we determined [42, 88]. The increasing electron density n_e in smaller tube diameters found in our experiments also complies with the simulation results [15, 19, 27]. On figure 5.14 (left) the line representing the $1/D$ dependence seems to fit the data for both positions quite nicely, though in a computational work the dependence has been suggested to be $1/D^2$ [19].

5.4.3. N_2 rotational temperature

The rotational temperature of N_2(C-B) was determined from the N_2 (C-B, 0-0) transition at 337.1 nm and N_2 (C-B, 0-2) transition at 380.5 nm as described in section 4.3.2. Due to the decrease of emission intensity, the uncertainty of temperature determination increased with the position downstream from the electrode. In the limits of accuracy, the temperature remained below 500 K in the whole used voltage range.

The dependence of rotational temperature of N_2(C-B) on applied voltage registered at 1 mm downstream from the electrode is shown in figure 5.15. The increase of temperature T_{rot} together with the applied voltages for all tube diameters is explainable by the increasing number of plasma pulses during a period of applied voltage which resulted in increased energy deposited into the discharge. At a given applied voltage the temperature T_{rot} decreased with decreasing tube diameter. For tube diameters 300 and 500 μm the temperature T_{rot} practically coincides. For smaller tube diameter, the temperature T_{rot} becomes smaller at same applied voltage.

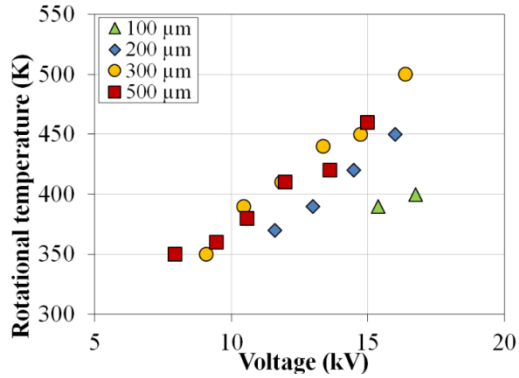

Figure 5.15. The N_2(C-B) rotational temperature as a function of the applied voltage for different tube diameters at 100 sccm. The temperatures were determined 1 mm downstream from the electrode.

5.5.4. He excitation temperature

He excitation temperature, T_{exc}, was determined from Boltzmann plot of various He emission lines as described in [**I**]. Figure 5.16 illustrates the change of He excitation temperature and normalized time-averaged intensity with tube diameter of 500 µm at 100 sccm flow rates. The excitation temperatures increased slightly with increasing voltage but the rise remained below the uncertainty of measurements (figure 5.16). The intensities of He lines on the other hand increased considerably. These results suggest that similarly to the electron density, the increasing number of pulses resulted in the increase of intensity while the average excitation temperature of a single pulse remained almost the same.

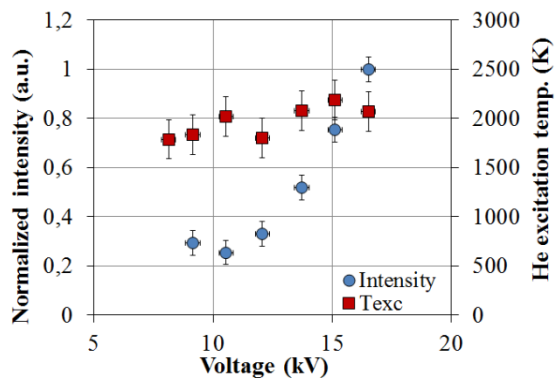

Figure 5.16. Time averaged normalized intensity and He excitation temperature as a function of applied voltage for 500 µm tube.

He excitation temperature obtained at constant voltage and flow rate can be seen to decrease from 2800 K to 2000 K with the increase of diameter from 80 µm to 500 µm (figure 5.17) which shows that the tube diameter is the main parameter determining the excitation temperature. It can be seen on figure 5.17 that the N_2 rotational temperature on the other hand increased with increasing tube diameter when other parameters were kept at the same value. The gas flow rate and the measurement position along the tube had also no clear effect on the excitation temperature.

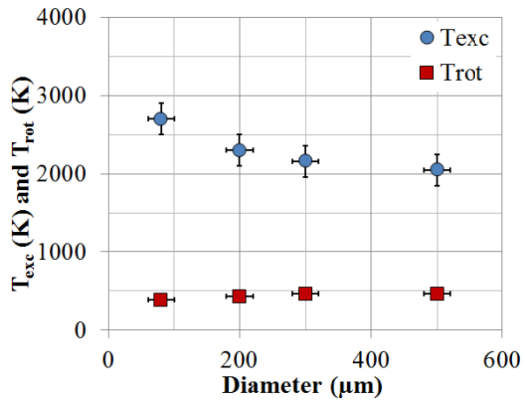

Figure 5.17. He excitation temperature (blue) and N_2 rotational temperature (red) as a function of dielectric tube diameter at 100 sccm measured 3 mm downstream from the electrode.

The values of excitation temperatures were similar to the values obtained in [42] but were an order of magnitude lower than the expected values of translational electron temperature T_e which should be between 10000 and 20000 K [14, 42, 87]. The discrepancy between T_{exc} and T_e is often observed in the case of helium based plasmas and is explained by strong deviation of the atomic state distribution function (ASDF) from thermodynamic equilibrium in ionizing plasmas (section 2.3.2). The difference in T_e and T_{exc} is explained by diffusion losses of charged particles which have to be compensated for by the over-population of lower levels.

5.5. Y-ZrO_2 microtubes

The effect of the dielectric tube material on the sustaining voltage and ionization wave velocity was tested with microtubes which were made from Y-ZrO_2 [89]. Yttria stabilized ZrO_2 is a material with high dielectric constant of 40 which is ten times higher than the dielectric constant of quartz. This results in increased capacitance of the dielectric tube and possibly also increases the surface charge density on the inner walls of the tube. The surface charge density in turn affects the ionization wave velocity according to several theoretical studies [16, 80].

We have performed some preliminary experiments to measure spectra along the tube axis and to determine the ionization wave velocity. Thorough characterization is not yet performed due to difficulties in producing Y-ZrO_2 microtubes with desirable diameter, length and quality. The smallest inner diameter of Y-ZrO_2 microtube which allowed to ignite the plasma was 50±5 µm (wall thickness 15±5 µm) but it was not possible to sustain the plasma for extended periods of time. Larger tubes with diameters in the range of 60–80 µm seemed to be more durable and easier to ignite but the production of such tubes was complicated. In addition to large diameter, the tube length of 10–15 mm is desirable for comparison of the results with the results obtained with quartz tubes but tubes having both large diameter and sufficient length were not available. It should also be pointed out that the few tubes which allowed to obtain the following results broke down structurally after 4–5 hours of working plasma but the reason is not known at this point.

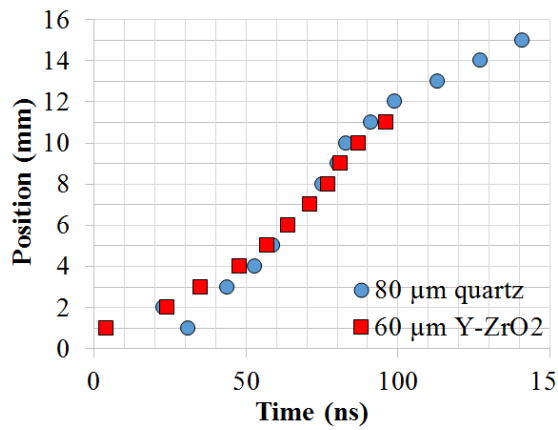

Figure 5.18. Temporal evolution of the ionization wave during the positive half period in a 60 µm Y-ZrO_2 microtube and in an 80 µm quartz tube. Flow rate was F_R= 10 and 20 sccm for Y-ZrO_2 and quartz tube, respectively.

Figure 5.18 shows the temporal evolution of the ionization wave along the discharge axis as a function of time for a 60 µm Y-ZrO_2 microtube and an 80 µm quartz tube during the positive half-cycle of applied voltage. It can be seen that in both cases the ionization wave was similarly accelerating inside the tube. Differently from the quartz tubes, in the case of the Y-ZrO_2 microtube the optical emission had a clear onset already at 2 mm from the powered electrode although the position uncertainty can be higher (maybe up to 1–2 mm). Outside from the tube the optical emission was recordable up to 4–5 mm in case of quartz tube and only 1–2 mm in case of the Y-ZrO_2 microtube. This can be explained by smaller length of the He jet caused by somewhat smaller tube diameter. The velocity of the ionization wave during its propagation in the tube (positions 5–10 mm) was 200 and 170 km/s for the quartz and Y-ZrO_2 microtube, respectively. These preliminary results suggest that higher dielectric constant results in smaller velocity of ionization wave in Y-ZrO_2 microtubes when compared to quartz tubes with same diameter especially when taking into account the expected increase of velocity when the tube diameter changes from 80 µm to 60 µm.

Figure 5.19 shows the comparison of the 667/728 nm line ratio in a 60 µm Y-ZrO_2 microtube and in a 60 µm quartz tube. In a 60 µm quartz tube the ratio was highest (approximately 10) near the powered electrode and fluctuated between 7.5 and 9 afterwards. It decreased closer to the tube orifice (positions 8–10). The 667/728 nm line ratio was about two times less in the Y-ZrO_2 microtube and varies between 4 and 6. It was constant for the most part along the axis and only a slight decrease can be observed near the tube orifice.

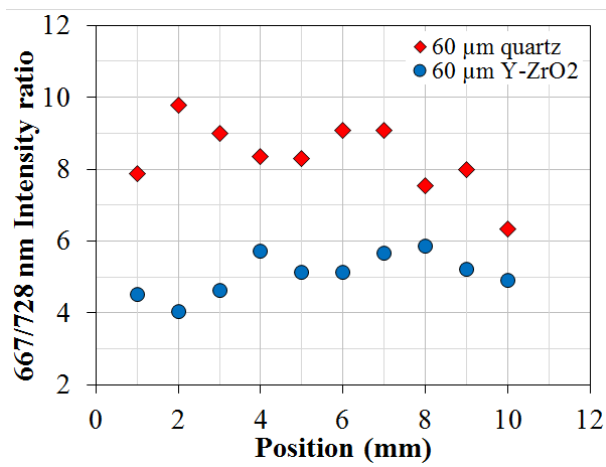

Figure 5.19. The 667/728 nm line intensity ratio along the discharge axis in a 60 µm Y-ZrO_2 microtube and in a 60 µm quartz tube. Flow rate was F_R= 10 and 20 sccm for Y-ZrO_2 and quartz tube, respectively.

6. OPEN PROBLEMS

Photographing of the ionization wave propagation at different positions along the tube axis with iCCD cameras is quite common in literature concerning APPJs [3]. This requires accurate triggering of the camera to precisely catch the short time window when the ionization wave is present in a certain position and collecting several hundred to thousand frames to increase total luminosity of the photograph. Concerning the tubes with diameters less than 500 μm that we have investigated the appearance of pulses from one half-cycle to the next half-cycle of the same polarity varies by 1–2 μs. method to reduce this jitter significantly has to be found to make the photographing the propagation of the ionization wave possible.

Spectral measurements separately for positive and negative voltage polarity would allow for a clear distinction how the tube diameter affects plasma parameters such as n_e, T_{rot} and T_{exc} depending on the voltage polarity. It might also prove possible to give an estimate of the time-averaged electric field during each half-cycle depending on the tube diameter.

It is likely that changing any of the experimental parameters such as ignition voltage waveform (e.g. from sinusoidal to pulsed dc), electrode geometry or the type of gas (e.g. from helium to argon) could have a significant effect on the dependencies of plasma parameters on the tube diameter as shown in this work.

In order to properly investigate the difference between the quartz and Y-ZrO_2 microtubes and the possible effect of dielectric constant of tube material more experiments must be performed with Y-ZrO_2 microtubes. The main problem during the experiments has been the large variability of the inner tube diameter, wall thickness and also the length of Y-ZrO_2 tubes (2–3 fold). Determination of plasma parameters including n_e, T_{rot} and T_{exc} is rather complicated as the total light intensity from such small discharge volume is low and to achieve reliable determination of those parameters the reproducibility of Y-ZrO_2 tubes with the exact same diameter and wall thickness is necessary.

An entirely uninvestigated problem is the influence of tube wall thickness. Increased wall thickness should increase the ignition voltage if other parameters (tube diameter, gas flow rate and electrode geometry) are not changed since the voltage drop inside the dielectric increases. We observed that some Y-ZrO_2 microtubes were not suitable at all to ignite plasma and we believe that one possible cause is the varying tube wall thickness.

7. SUMMARY

The main aim of the thesis was to investigate the effect of dielectric tube diameter (80–500 μm) on atmospheric pressure plasma jet characteristics such as sustaining voltage, ionization wave velocity and plasma parameters such as electron density, gas temperature and He excitation temperature. The time-averaged electron density, gas temperature and He excitation temperature were determined from the Stark broadening of the H_β line, the N_2 rotational temperature and intensities of spectral lines of He, respectively. Ionization wave velocity was determined from the temporal delay of the optical emission corresponding to the travelling ionization wave at consecutive positions along the tube axis.

The main results of this work are as follows:

- Ignition and sustaining voltage increase with decreasing tube diameter. The increase is attributed to the increased losses of charged species to the tube walls which have to be compensated for by increased ionization as a result of stronger applied electric field.
- Electron density and He excitation temperature increase while the N_2 rotational temperature decreases with decreasing tube diameter. The tube diameter had stronger effect on these plasma parameters when compared to applied voltage or flow rate.
- Ionization wave velocity increases with decreasing tube diameter for both voltage polarities. The increased velocity can be attributed to stronger electric field during the breakdown and propagation of the ionization wave.
- It was determined that within a few kilovolts above the sustaining voltage a single ionization wave occurs each half-cycle of applied voltage and its characteristics depend only weakly on the applied voltage and flow rate. With increasing voltage the number of ionization waves observed during each half-period increases monotonically. The consecutive ionization wave start travelling from the tube exit instead of the high-voltage electrode.

8. SUMMARY IN ESTONIAN

Dielektriktoru diameetri mõju atmosfääri rõhul töötava He plasmajoa parameetritele

Atmosfäärirõhul töötav plasmajuga tekitatakse dielektriktorust väljuvas inertgaasi joas, rakendades kõrgepinge elektroodile vahelduvpinge. Kui kasutatava vahelduvpinge sagedus on kilohertside suurusjärgus, koosneb plasmajuga kuni 1 μs kestusega ionisatsioonilainetest, mis levivad kiirusega kuni 10^3 km/s. Sellistest ionisatsioonilainetest koosnev plasmajuga on madalatel temperatuuridel töötav efektiivne keemiliselt aktiivsete ühendite allikas ja seetõttu on neid seadmeid viimase kümnendi vältel uuritud intensiivselt biomeditsiini rakendustes.

Biomeditsiini rakendused eeldavad täpset kontrolli plasma parameetrite üle. Ionisatsioonilainete kiirust ja plasma karakteristikuid, nagu näiteks elektronide tihedus, elektronide temperatuur ning gaasi temperatuur, on võimalik kontrollida rakendatava pinge kuju ning amplituudiga, gaasi koostisega, gaasivoo kiirusega ja ka elektroodide konfiguratsiooniga. Dielektriktoru diameetri muutmine võib anda veel ühe võimaluse plasma parameetrite kontrollimiseks, kuid seniajani ei ole sellel teemal süstemaatilisi uuringuid tehtud.

Käesoleva doktoritöö eesmärgiks oli määratleda dielektriktoru diameetri mõju plasma kustumispingele, elektronide arvtihedusele, gaasi temperatuurile, He ergastustemperatuurile ja ionisatsioonilaine kiirusele He atmosfääri rõhul töötavas plasmajoas. Dielektrikutoru diameetrit muudeti vahemikus 80–500 μm. Elektronide arvtihedus, gaasi temperatuur ning He ergastustemperatuur määrati spektroskoopia meetoditega vastavalt H_β joone Starki laienemisest, N_2 rotatsioontemperatuurist ning He joonte intensiivsustest. Ionisatsioonilainete kiirus määrati voolupulsi ja optilise kiirguse vahelise ajalise nihke muutusest piki toru telge iga millimeetri tagant.

Töö peamised tulemused on:

- Plasma süttimis- ja kustumispinge kasvab dielektriktoru diameetri vähenedes. Kasvu põhjusena võib tuua laengukandjate difusioonikao kasvu toru seintele. Selle kao kompenseerimiseks on vaja suurendada ionisatsiooni, mis saavutatakse tugevama rakendatava elektriväljaga.
- Elektronide tihedus ning He ergastustemperatuur kasvavad toru diameetri vähenedes ning samas gaasi temperatuuri iseloomustav N_2 rotatsioontemperatuur väheneb. Toru diameetri mõju neile parameetritele oli kasutatud plasmajoa kontsentratsiooni korral olulisem kui rakendatud pinge amplituud või gaasivoo kiirus.
- Ionisatsioonilaine kiirus kasvab samuti dielektriktoru diameetri vähenedes. Selle põhjuseks on tugevam elektriväli ionisatsioonilaine peas.
- Kõigi kasutatud toru diameetrite korral tekib lävepinge lähedastel pingetel iga poolperioodi jooksul üks ionisatsioonilaine, mille parameetrid (leviku kiirus, kiirendus) praktiliselt ei sõltu rakendatud pinge amplituudväärtusest. Teatavast pinge amplituudväärtusest (~2-3 kV lävepingest kõrgemal)

kõrgemal tekib ühes poolperioodis kaks või enam ionisatsioonilainet. Seejuures liigub esimene ionisatsioonilaine kõrgepinge elektroodist toru otsa suunas ning järgnevad ionisatsioonilained initsieeritakse hoopis toru otsa lähedal ning levivad sealt kahes suunas.

REFERENCES

[1] X. Lu and M. Laroussi, Dynamics of an atmospheric pressure plasma plume generated by submicrosecond voltage pulses, *J. Appl. Phys.* **100** (2006) 063302

[2] M. Laroussi, Low Temperature Plasma Jet for Biomedical Applications: A Review, *IEEE Trans. Plasma Sci.* **43** (2015) 703–711

[3] X. Lu, G. V. Naidis, M. Laroussi and K. Ostrikov, Guided ionization waves: Theory and experiments, *Phys. Rep.* **540** (2014) 123–166

[4] M. G. Kong, G. Kroesen, G. Morfill, T. Nosenko, T. Shimizu, J. van Dijk and J. L. Zimmermann, Plasma medicine: an introductory review, *New J. Phys.* **11** (2009) 115012

[5] B. Haertel, T. von Woedtke, K.-D. Weltmann and U. Lindequist, Non-thermal atmospheric-pressure plasma possible application in wound healing, *Biomol. Ther.* **22** (2014) 477–490

[6] A.V. Nastuta, I. Topala, C. Grigoras, V. Pohoata and G. Popa, Stimulation of wound healing by helium atmospheric pressure plasma treatment, *J. Phys. D. Appl. Phys.* **44** (2011) 105204

[7] M. Keidar, R. Walk, A. Shashurin, P. Srinivasan, A. Sandler, S. Dasgupta, R. Ravi, R. Guerrero-Preston and B. Trink, Cold plasma selectivity and the possibility of a paradigm shift in cancer therapy, *British J. Canc*er **105** (2011) 101032

[8] M. Keidar, A. Shashurin, O. Volotskova, M. A. Stepp, P. Srinivasan, A. Sandler and B. Trink, Cold atmospheric plasma in cancer therapy, *Phys. Plasmas* **20** (2013) 101063

[9] S. Bornholdt, M. Wolter and H. Kersten, Characterization of an atmospheric pressure plasma jet for surface modification and thin film deposition, *Eur. Phys. J. D.* **60** (2010) 653–660

[10] K. G. Kostov, T. M. C. Nishime, A. H. R. Castro, A. Toth and L. R. O. Hein, Surface modification of polymeric materials by cold atmospheric plasma jet, *Appl. Surf. Sci.* **314** (2014) 367–375

[11] D. Mariotti and R. M. Sankaran, Microplasmas for nanomaterials synthesis, *J. Phys. D. Appl. Phys.* **43** (2010) 323001

[12] N. Mericam-Bourdet, M. Laroussi, A. Begum and E. Karakas, Experimental investigations of plasma bullets, *J. Phys D. Appl. Phys.* **42** (2009) 055207

[13] D. Mariotti, Nonequilibrium and effect of gas mixtures in an atmospheric microplasma, *Appl. Phys. Lett.* **92** (2008) 151505

[14] J. Jonkers, M. Sande, A. Sola, A. Gamero and J. Mullen, On the differences between ionizing helium and argon plasmas at atmospheric pressure, *Plasma Sources Sci. Technol.* **12** (2003), 30

[15] J. Jansky, F. Tholin, Z. Bonaventura and A. Bourdon, Simulation of the discharge propagation in a capillary tube in air at atmospheric pressure, *J. Phys. D Appl. Phys.* **43** (2010) 395201

[16] J. Jansky, P. Delliou, F. Tholin, P. Tardiveau, A. Bourdon, S. Pasquiers, Experimental and numerical study of the propagation of a discharge in a capillary tube in air at atmospheric pressure, *J. Phys. D- Appl. Phys.* **44** (2011) 335201

[17] N. Puač, D. Maletić, S. Lazović, G. Malović, A. Dordević and Z.L. Petrović, Time resolved optical emission images of an atmospheric pressure plasma jet with transparent electrodes, *Appl. Phys. Lett.* **101** (2012) 024103

[18] J. Jarrige, M. Laroussi and E. Karakas, Formation and dynamics of plasma bullets in a non-thermal plasma jet: influence of the high-voltage parameters on the plume characteristics, *Plasma Sources Sci. Technol.* **19** (2010) 065005
[19] J. P. Boeuf, L. L. Yang and L. C. Pitchford, Dynamics of a guided streamer ('plasma bullet') in a helium jet in air at atmospheric pressure, *J. Phys. D: Appl. Phys.* **46** (2013) 015201
[20] X. Lu, M. Laroussi, V. Puech, On atmospheric-pressure non-equilibrium plasma jets and plasma bullets, *Plasma Sources. Sci. Technol.* **21** (2012) 034005
[21] J.L. Walsh and M.G. Kong, Contrasting characteristics of linear-field and cross-field atmospheric plasma jets, *Appl. Phys. Lett.* **93** (2008) 111501
[22] K. McKay, J.-S. Oh, J. L. Walsh and J. W. Bradley, Mass spectrometric diagnosis of an atmospheric pressure helium microplasma jet, *J. Phys. D. Appl. Phys.* **46** (2013) 464018
[23] G. V. Naidis, Simulation of streamers propagating along helium jets in ambient air: Polarity-induced effects, *Appl. Phys. Lett.* **98** (2011) 141501
[24] R. Xiong, Q. Xiong, A. Nikiforov, P. Vanraes and C. Leys, Influence of helium mole fraction distribution on the properties of cold atmospheric pressure helium plasma jets, *J. Appl. Phys.* **112** (2012) 033305
[25] J. Jansky and A. Bourdon, Simulation of helium discharge ignition and dynamics in thin tubes at atmospheric pressure, *Appl. Phys. Lett.* **99** (2011) 161504
[26] H. Cheng, X. Lu and D. Liu, The Effect of Tube Diameter on an Atmospheric-Pressure Micro-Plasma Jet, *Plasma Process. Polym.* **12** (2015) 1343–1347
[27] D. Breden, K. Miki and L.L. Raja, Self-consistent two-dimensional modeling of cold atmospheric-pressure plasma jets/bullets, *Plasma Sources Sci. Technol.* **21.** (2012) 034011
[28] A. Friedman and L. A. Kennedy, Plasma physics and engineering, *CRC Press* 2011
[29] Y. P. Raizer, Gas discharge physics, *Springer Verlag* (1991)
[30] G. A. Dawson and W. P. Winn, A model for streamer propagation, *Z. Physik* **183 (**1965) 159–171
[31] R. D. Klingbeil, A. Tidman and R. F. Fernsler. Ionizing gas breakdown waves in strong electric fields. *Phys. Fluids* **15** (1969)
[32] E. D. Lozansky and O. B. Firsov. Theory of Sparks, *Atom-izdat* (1975)
[33] E. Karakas, M.A. Akman and M. Laroussi, The evolution of atmospheric-pressure low-temperature plasma jets: jet current measurements, *Plasma Sources Sci. Technol.* **21** (2012) 034016
[34] G. B. Sretenović, I. B. Krstić, V. V. Kovačević, B. M. Obradović, M. M. Kuraica, Spatio-temporally resolved electric field measurements in helium plasma jet, *J. Phys. D: Appl. Phys.* **47** (2014) 102001
[35] T. Shao, C. Zhang, R. Wang, Y. Zhou, Q. Xie and Z. Fang, Comparison of atmospheric-pressure He and Ar plasma jets driven by microsecond pulses, *IEEE Trans. Plasma Sci.* **43** (2015) 726–732
[36] E. Karakas and M. Laroussi, Experimental studies on the plasma bullet propagation and its inhibition, *J. Appl. Phys.* **108** (2010) 063305
[37] C. Jiang, M. T. Chen and M. A. Gundersen, Polarity-induced asymmetric effects of nanosecond pulsed plasma jets, *J. Phys. D. Appl. Phys.* **42** (2009) 232002
[38] Q. Xiong, X. Lu, Y. Xian, J. Liu, C. Zou, Z, Xiong, W. Gong, K. Chen, X. Pei, F. Zou, J. Hu, Z. Jiang and Y. Pan, Experimental investigations on the propagation of the plasma jet in the open air, *J. Appl. Phys.* **107** (2010) 073302

[39] J.L. Walsh, P. Olszewski and J.W. Bradley, The manipulation of atmospheric pressure dielectric barrier plasma jets, *Plasma Sources Sci. Technol.* **21** (2012) 034007
[40] W. Ning, L. Wang, C. Wu and S. Jia, Influence of voltage magnitude on the dynamic behavior of a stable helium atmospheric pressure plasma jet, *J. Appl. Phys.* **116** (2014) 073301
[41] Q. Xiong, X. Lu, K. Ostrikov, Y. Xian, C. Zou, Z. Xiong and Y. Pan, Pulsed dc- and sine-wave-excited cold atmospheric plasma plumes: A comparative analysis, *Phys. Plasmas.* **17** (2010) 043506
[42] V. N. Ochkin, Spectroscopy of Low Temperature Plasma, *Wiley-VCH* 2009
[43] J. Jonkers and J.A.M. Mullen, The excitation temperature in (helium) plasmas, *J. Quant. Spectrosc. Radiat. Transfer* **61** (1999) 703–709
[44] T. Fujimoto, Plasma spectroscopy, *Claredon press* 2004
[45] Q. Xiong, A. Y. Nikiforov, M. A. Gonzalez, C. Leys, X. P. Lu, Characterization of an atmospheric helium plasma jet by relative and absolute optical emission spectroscopy, *Plasma Sources Sci. Technol.* **22** (2012) 015011
[46] A. Friedman, Plasma chemistry, *Cambridge University press* 2008
[47] K. Niemi, T. Gans and D. O'Connell, Comparison of a global model to semi-kinetic fluid simulations for atmospheric pressure radio-frequency plasmas, *Plasma. Sources. Sci. Technol.* **22** (2013) 032001
[48] D. B. Graves, The emerging role of reactive oxygen and nitrogen species in redox biology and some implications for plasma applications to medicine and biology, *J. Phys. D. Appl. Phys.* **45** (2012) 263001
[49] X. Pei, Y. Lu, S. Wu, Q. Xiong and X. Lu, A study on the temporally and spatially resolved OH radical distribution of a room-temperature atmospheric-pressure plasma jet by laser-induced fluorescence imaging, *Plasma Sources Sci. Technol.* **22** (2013) 025023
[50] S. Yonemori and R. Ono, Flux of OH and O radicals onto a surface by an atmospheric-pressure helium plasma jet measured by laser-induced fluorescence, *J. Phys. D: Appl. Phys.* **47** (2014) 125401
[51] S. Yonemori, Y. Nakagawa, R. Ono and T. Oda, Measurement of OH density and air-helium mixture ratio in atmospheric-pressure helium plasma jet, *J. Phys. D: Appl. Phys.* **45** (2012) 225202
[52] M. Laroussi, Low Temperature Plasma-Based Sterilization: Overview and State-of-the-Art, *Plasma Process. Polym.* **2** (2005) 391–400
[53] M. Keidar, R. Walk, A. Shashurin, P. Srinivasan, A. Sandler, S. Dasgupta, R. Ravi, R. Guerrero-Preston and B. Trink, Cold plasma selectivity and the possibility of a paradigm shift in cancer therapy, *Br. J. Canc*er **105** (2011) 1295–12301
[54] M. Keidar, Plasma for cancer treatment, *Plasma Sources Sci. Technol.* **24** (2015) 033001
[55] P. Babington, K. Rajjoub, J. Canady, A. Siu, M. Keidar and J. H. Sherman, Use of cold atmospheric plasma in the treatment of cancer, *Biointerphases* **10** (2015) 029403
[56] A. Grill, Cold Plasma in Materials Fabrication – from Fundamentals to Applications, *IEEE Press* 1994
[57] M. J. Shenton and G. C. Stevens, Surface modification of polymer surfaces: atmospheric plasma versus vacuum plasma treatments, *J. Phys. D. Appl. Phys.* **34** (2001) 2761–2768

[58] K. Ostrikov, E. C. Neyts and M. Meyyappan, Plasma nanoscience: from nano-solids in plasmas to nano-plasmas in solids, *Adv. Phys.* **62** (2013) 113–224
[59] J. Kang, O. L. Li and N. Saito, Synthesis of structure-controlled carbon nanospheres by solution plasma process, *Carbon* **60** (2013) 292–298
[60] M. V. Jacob, R. S. Rawat, B. Ouyang, K. Bazaka, D. S. Kumar, D. Taguchi, M. Iwamoto, R. Neupane and O. K. Varghese, Catalyst-Free Plasma Enhanced Growth of Graphene from Sustainable Sources, *Nano Lett.* **15** (2015) 5702–5708
[61] J. Fang, I. Levchenko and K. Ostrikov, Atmospheric plasma jet-enhanced anodization and nanoparticle synthesis, *IEEE Trans. Plasma Sci.* **43** (2015) 765–769
[62] M. Noeske, J. Degenhardt, S. Strudthoff and U. Lommatzsch, Plasma jet treatment of five polymers at atmospheric pressure: Surface modifications and the relevance for adhesion, *Inter. J. Adhesion Adhesives* **24** (2004) 171–177
[63] U. Lommatzsch, D. Pasedag, A. Baalmann, G. Ellinghorst and H.-E. Wagner, Atmospheric Pressure Plasma Jet Treatment of Polyethylene Surfaces for Adhesion Improvement, *Plasma Process. Polym.* **4** (2007) S1041–S1045
[64] K. G. Kostov, T. M. C. Nishime, A. H. R. Castro, A. Toth and L. R. O. Hein, Surface modification of polymeric materials by cold atmospheric plasma jet, *Appl. Surface Sci.* **314** (2014) 367–375
[65] T. Takamatsu, H. Hirai, R. Sasaki, H. Miyahara and A. Okino, Surface Hydrophilization of Polyimide Films Using Atmospheric Damage-Free Multigas Plasma Jet Source, *IEEE Trans. Plasma Sci.* **41** (2013) 119–125
[66] S. Kalia, K. Thakur, A. Celli, M. A. Kiechel and C. L. Schauer, Surface modification of plant fibers using environment friendly methods for their application in polymer composites, textile industry and antimicrobial activities: a review, *J. Environ. Chem. Eng.* **1** (2013) 97–112
[67] A. Zille, F. R. Oliveira and A. P. Suoto, Plasma treatment in textile industry, *Plasma Process. Polym.* **12** (2015) 98–131
[68] R. Morent, N. de Geyter, T. Desmet, P. Dubruel and C. Leys, Plasma surface modification of biodegradable polymers: a review, *Plasma Process. Polym.* **8** (2011) 171–190
[69] F. Massines, C. Sarra-Bournet, F. Fanelli, N. Naudé and N. Gherardi, Atmospheric pressure low temperature direct plasma technology: status and challenges for thin film deposition, *Plasma Process. Polym.* **9** (2012) 1041–1073
[70] T. Belmonte, G. Henrion and T. Gries, Nonequilibrium Atmospheric Plasma Deposition, *J. Therm. Spray Technol.* **20** (2011) 744–759
[71] U. Fantz, Basics of plasma spectroscopy, *Plasma Sources Sci. Technol.* **15** (2006) S137-S147
[72] N. Konjević, M. Ivković, and N. Sakan, Hydrogen Balmer lines for low electron number density plasma diagnostics, *Spectrochim. Acta B* **76** (2012) 16–26
[73] C. O. Laux, T. G. Spence, C. H. Kruger and R. N. Zare, Optical diagnostics of atmospheric pressure air plasmas, *Plasma Sources Sci. Technol.* **12** (2003) 125–138
[74] M. A. Gigosos and V. Cardenoso, New plasma diagnosis tables of hydrogen Stark broadening including ion dynamics, *J. Phys. B. At. Mol. Opt. Phys.* **29** (1996) 4795–4838
[75] G. B. Sretenović, I. B. Krstić, V. V. Kovačević, B. M. Obradević and M. M. Kuraica, Spectroscopic measurement of electric field in atmospheric-pressure plasma jet operating in bullet mode, *Appl. Phys. Lett.* **99** (2011) 161502

[76] S.S. Ivković, G.B. Sretenović, B.M. Obradović, N. Cvetanović and M.M. Kuraica, On the use of the intensity ratio of He lines for electric field measurements in atmospheric pressure dielectric barrier discharge, *J. Phys. D. Appl. Phys.* **47** (2014) 055204
[77] T. Hoder, D. Loffhagen, J. Voráč, M. M. Becker and R. Brandenburg, Analysis of the electric field development and the relaxation of electron velocity distribution function for nanosecond breakdown in air, *Plasma Sources Sci. Technol.* **25** (2016) 025017
[78] V. Repän, Low Current Mode of Negative Corona, *Dissertationes Physicae Universitatis Tartuensis* **42** Tartu (2004)
[79] Q. Xiong, X. Lu, J. Liu, Y. Xian, Z. Xiong, F. Zou, C. Zou, W. Gong, J. Hu, K. Chen, X. Pei, Z. Jiang and Y. Pan, Temporal and spatial resolved optical emission behaviors of a cold atmospheric pressure plasma jet, *J. Appl. Phys.* **106** (2009) 083302
[80] M. D. S. Mussard, O. Guaitella and A. Rousseau, Propagation of plasma bullets in helium within a dielectric capillary – influence of the interaction with surfaces, *J. Phys. D: Appl. Phys.* **46** (2013) 302001
[81] J. Jansky and A. Bourdon, Surface charge deposition inside a capillary glass tube by an atmospheric pressure discharge in air, *Eur. Phys. J. Appl. Phys.* **55** (2011) 13810
[82] A. A. Kulikovsky, Positive streamer in a weak field in air: A moving avalanche-to-streamer transition, *Phys. Rev. E* **57** (1998) 7066–7074
[83] G. E. Georghiou, A. P. Papadakis, R. Morrow and A. C. Metaxas, Numerical modeling of atmospheric pressure gas discharges leading to plasma production, *J. Phys. D: Appl. Phys.* **38** (2005) R303–E328
[84] K. Hensel, V. Martišovitš, Z. Machala, M. Janda, M. Leštinský, P. Tardiveau and A, Mizuno, Electrical and optical properties of AC microdischarges in porous ceramics, *Plasma Process. Polym.* **4** (2007) 682–693
[85] Z. Chang, N. Jiang, G. Zhang and Z. Cao, Influence of Penning effect on the plasma features in a non-equilibrium atmospheric pressure plasma jet, *J. Appl. Phys.* **115** (2014) 103301
[86] X. Y. Liu, X. K. Pei, X. P. Lu and D.W. Liu, Numerical and experimental study on a pulsed-dc plasma jet, *Plasma Sources Sci. Technol.* **23** (2014) 035007
[87] J. Jonkers, M. Sande, A. Sola, A. Gamero and J.A.M. Mullen, On the differences between ionizing helium and argon plasmas at atmospheric pressure, *Plasma Sources Sci. Technol.* **12** (2003) 30–38
[88] J. Jánský, W. T. Algwari, D. O'Connell and A. Bourdon, Experimental-Modeling Study of an Atmospheric-Pressure Helium Discharge Propagation in a Thin Dielectric Tube, *IEEE Trans. Plasma Sci.* **40** (2012) 2912–2919
[89] T. Tätte. M. Part, R. Talviste, K. Hanschmidt, K. Utt, U. Mäeorg, I. Jõgi, V. Kiisk, H. Mändar, G. Nurk and P. Rauwell, Yttria stabilized zirconia microtubes for microfluidics under extreme conditions, RSC Advances **34** (2014) 17413–17419

ACKNOWLEDGMENTS

First and foremost I would like to thank my supervisor Indrek Jõgi for supervising the work and his continued insight and patience. Secondly, I would like to thank the laboratory engineer Tõnu Asu who made it at all possible to measure plasma inside sub-millimeter tubes. Thirdly, my sincere thanks go to all the members of the Gas Discharge Laboratory at the University of Tartu for all the useful advice over the years. Finally, I would also like to thank my parents for their ongoing support.

PUBLICATIONS

CURRICULUM VITAE

Name: Rasmus Talviste
Date of birth: August 20, 1984
Nationality: Estonian
Phone: +372 53486237
E-mail: rass.talviste@gmail.com; rasmus.talviste@ut.ee

Education:
2012 Tallinn Technical University, MSc *cum laude* (Material technology)
2007 University of Tartu, BSc (Material Science)
2003 Tallinn Mustamäe Gymnasium

Languages:
Estonian
English
German

Research activity:
1) Main research area:
– Atmospheric pressure plasmas
2) List of publications:
– Jõgi, R. Talviste, J. Raud, K. Piip and P. Paris. (2014) "The influence of the tube diameter on the properties of an atmospheric pressure He micro-plasma jet". *Journal of Physics D: Applied physics,* **47**, 415202 – Article I
– R. Talviste, I. Jõgi, J. Raud and P. Paris. (2016) "Development of ionization waves in an atmospheric-pressure micro-plasma jet". *Contributions to plasma physics,* **56**, 101002 – Article II
– R. Talviste, I. Jõgi, J. Raud and P. Paris. (2016) "The effect of dielectric tube diameter on the propagation velocity of ionization waves in a He atmospheric-pressure micro-plasma jet". ". *Journal of Physics D: Applied physics,* **49**, 195201 – Article III
– T. Tätte. M. Part, R. Talviste, K. Hanschmidt, K. Utt, U. Mäeorg, I. Jõgi, V. Kiisk, H. Mändar, G. Nurk and P. Rauwell. (2014) "Yttria stabilized zirconia microtubes for microfluidics under extreme conditions". *RSC advances,* **34**, 101039
– T. Tätte, M. Paalo, M. Part, R. Talviste, V. Kiisk, H. Mändar, K. Põhako, T. Pehk, K. Reivelt, M. Natali, J. Gurauskis, A. Lõhmus and U. Mäeorg. (2011) "Alkoxide-based precursors for direct drawing of metal oxide micro- and nanofibers". *Science and Technology of Advanced Materials*, **12**, 034412
– T. Tätte A. Kolesnikova, M. hussainov, R. Talviste, R. Lõhmus, A. Romanov, I. Hussainova and A. Lõhmus. (2010) "Crack formation during post-treatment of nano- and microfibers by sol-gel technique". *Journal of Nanoscience and Nanotechnology*, **10**, 101166

ELULOOKIRJELDUS

Nimi: Rasmus Talviste
Sünniaeg: 20. august, 1984
Rahvus: Eestlane
Telefon: +372 5348 6237
E-post: rass.talviste@gmail.com; rasmus.talviste@ut.ee

Haridustee:
2012 Tallinn Tehnikaülikool, MSc *cum laude* (Materjalide tehnoloogia)
2007 Tartu Ülikool, BSc (Materjaliteadus)
2003 Tallinn Mustamäe Gümnaasium

Keelteoskus:
Eesti
Inglise
Saksa

Teadustegevus:
1) Peamine uurimisvaldkond:
– Atmosfääri rõhul plasma
2) Publikatsioonide loetelu:
– Jõgi, R. Talviste, J. Raud, K. Piip and P. Paris. (2014) "The influence of the tube diameter on the properties of an atmospheric pressure He micro-plasma jet". *Journal of Physics D: Applied physics,* **47**, 415202 – Article I
– R. Talviste, I. Jõgi, J. Raud and P. Paris. (2016) "Development of ionization waves in an atmospheric-pressure micro-plasma jet". *Contributions to plasma physics,* **56**, 101002 – Article II
– R. Talviste, I. Jõgi, J. Raud and P. Paris. (2016) "The effect of dielectric tube diameter on the propagation velocity of ionization waves in a He atmospheric-pressure micro-plasma jet". ". *Journal of Physics D: Applied physics,* **49**, 195201 – Article III
– T. Tätte. M. Part, R. Talviste, K. Hanschmidt, K. Utt, U. Mäeorg, I. Jõgi, V. Kiisk, H. Mändar, G. Nurk and P. Rauwell. (2014) "Yttria stabilized zirconia microtubes for microfluidics under extreme conditions". *RSC advances,* **34**, 101039
– T. Tätte, M. Paalo, M. Part, R. Talviste, V. Kiisk, H. Mändar, K. Põhako, T. Pehk, K. Reivelt, M. Natali, J. Gurauskis, A. Lõhmus and U. Mäeorg. (2011) "Alkoxide-based precursors for direct drawing of metal oxide micro- and nanofibers". *Science and Technology of Advanced Materials*, **12**, 034412
– T. Tätte A. Kolesnikova, M. hussainov, R. Talviste, R. Lõhmus, A. Romanov, I. Hussainova and A. Lõhmus. (2010) "Crack formation during post-treatment of nano- and microfibers by sol-gel technique". *Journal of Nanoscience and Nanotechnology*, **10**, 101166

DISSERTATIONES PHYSICAE UNIVERSITATIS TARTUENSIS

1. **Andrus Ausmees.** XUV-induced electron emission and electron-phonon interaction in alkali halides. Tartu, 1991.
2. **Heiki Sõnajalg.** Shaping and recalling of light pulses by optical elements based on spectral hole burning. Tartu, 1991.
3. **Sergei Savihhin.** Ultrafast dynamics of F-centers and bound excitons from picosecond spectroscopy data. Tartu, 1991.
4. **Ergo Nõmmiste.** Leelishalogeniidide röntgenelektronemissioon kiiritamisel footonitega energiaga 70–140 eV. Tartu, 1991.
5. **Margus Rätsep.** Spectral gratings and their relaxation in some low-temperature impurity-doped glasses and crystals. Tartu, 1991.
6. **Tõnu Pullerits.** Primary energy transfer in photosynthesis. Model calculations. Tartu, 1991.
7. **Olev Saks.** Attoampri diapasoonis voolude mõõtmise füüsikalised alused. Tartu, 1991.
8. **Andres Virro.** AlGaAsSb/GaSb heterostructure injection lasers. Tartu, 1991.
9. **Hans Korge.** Investigation of negative point discharge in pure nitrogen at atmospheric pressure. Tartu, 1992.
10. **Jüri Maksimov.** Nonlinear generation of laser VUV radiation for high-resolution spectroscopy. Tartu, 1992.
11. **Mark Aizengendler.** Photostimulated transformation of aggregate defects and spectral hole burning in a neutron-irradiated sapphire. Tartu, 1992.
12. **Hele Siimon.** Atomic layer molecular beam epitaxy of A^2B^6 compounds described on the basis of kinetic equations model. Tartu, 1992.
13. **Tõnu Reinot.** The kinetics of polariton luminescence, energy transfer and relaxation in anthracene. Tartu, 1992.
14. **Toomas Rõõm.** Paramagnetic H^{2-} and F^+ centers in CaO crystals: spectra, relaxation and recombination luminescence. Tallinn, 1993.
15. **Erko Jalviste.** Laser spectroscopy of some jet-cooled organic molecules. Tartu, 1993.
16. **Alvo Aabloo.** Studies of crystalline celluloses using potential energy calculations. Tartu, 1994.
17. **Peeter Paris.** Initiation of corona pulses. Tartu, 1994.
18. **Павел Рубин.** Локальные дефектные состояния в CuO_2 плоскостях высокотемпературных сверхпроводников. Тарту, 1994.
19. **Olavi Ollikainen.** Applications of persistent spectral hole burning in ultrafast optical neural networks, time-resolved spectroscopy and holographic interferometry. Tartu, 1996.
20. **Ülo Mets.** Methodological aspects of fluorescence correlation spectroscopy. Tartu, 1996.
21. **Mikhail Danilkin.** Interaction of intrinsic and impurity defects in CaS:Eu luminophors. Tartu, 1997.

22. **Ирина Кудрявцева.** Создание и стабилизация дефектов в кристаллах KBr, KCl, RbCl при облучении ВУФ-радиацией. Тарту, 1997.
23. **Andres Osvet.** Photochromic properties of radiation-induced defects in diamond. Tartu, 1998.
24. **Jüri Örd.** Classical and quantum aspects of geodesic multiplication. Tartu, 1998.
25. **Priit Sarv.** High resolution solid-state NMR studies of zeolites. Tartu, 1998.
26. **Сергей Долгов.** Электронные возбуждения и дефектообразование в некоторых оксидах металлов. Тарту, 1998.
27. **Kaupo Kukli.** Atomic layer deposition of artificially structured dielectric materials. Tartu, 1999.
28. **Ivo Heinmaa.** Nuclear resonance studies of local structure in $RBa_2Cu_3O_{6+x}$ compounds. Tartu, 1999.
29. **Aleksander Shelkan.** Hole states in CuO_2 planes of high temperature superconducting materials. Tartu, 1999.
30. **Dmitri Nevedrov.** Nonlinear effects in quantum lattices. Tartu, 1999.
31. **Rein Ruus.** Collapse of 3d (4f) orbitals in 2p (3d) excited configurations and its effect on the x-ray and electron spectra. Tartu, 1999.
32. **Valter Zazubovich.** Local relaxation in incommensurate and glassy solids studied by Spectral Hole Burning. Tartu, 1999.
33. **Indrek Reimand.** Picosecond dynamics of optical excitations in GaAs and other excitonic systems. Tartu, 2000.
34. **Vladimir Babin.** Spectroscopy of exciton states in some halide macro- and nanocrystals. Tartu, 2001.
35. **Toomas Plank.** Positive corona at combined DC and AC voltage. Tartu, 2001.
36. **Kristjan Leiger.** Pressure-induced effects in inhomogeneous spectra of doped solids. Tartu, 2002.
37. **Helle Kaasik.** Nonperturbative theory of multiphonon vibrational relaxation and nonradiative transitions. Tartu, 2002.
38. **Tõnu Laas.** Propagation of waves in curved spacetimes. Tartu, 2002.
39. **Rünno Lõhmus.** Application of novel hybrid methods in SPM studies of nanostructural materials. Tartu, 2002.
40. **Kaido Reivelt.** Optical implementation of propagation-invariant pulsed free-space wave fields. Tartu, 2003.
41. **Heiki Kasemägi.** The effect of nanoparticle additives on lithium-ion mobility in a polymer electrolyte. Tartu, 2003.
42. **Villu Repän.** Low current mode of negative corona. Tartu, 2004.
43. **Алексей Котлов.** Оксианионные диэлектрические кристаллы: зонная структура и электронные возбуждения. Tartu, 2004.
44. **Jaak Talts.** Continuous non-invasive blood pressure measurement: comparative and methodological studies of the differential servo-oscillometric method. Tartu, 2004.
45. **Margus Saal.** Studies of pre-big bang and braneworld cosmology. Tartu, 2004.

46. **Eduard Gerškevitš.** Dose to bone marrow and leukaemia risk in external beam radiotherapy of prostate cancer. Tartu, 2005.
47. **Sergey Shchemelyov.** Sum-frequency generation and multiphoton ionization in xenon under excitation by conical laser beams. Tartu, 2006.
48. **Valter Kiisk.** Optical investigation of metal-oxide thin films. Tartu, 2006.
49. **Jaan Aarik.** Atomic layer deposition of titanium, zirconium and hafnium dioxides: growth mechanisms and properties of thin films. Tartu, 2007.
50. **Astrid Rekker.** Colored-noise-controlled anomalous transport and phase transitions in complex systems. Tartu, 2007.
51. **Andres Punning.** Electromechanical characterization of ionic polymer-metal composite sensing actuators. Tartu, 2007.
52. **Indrek Jõgi.** Conduction mechanisms in thin atomic layer deposited films containing TiO_2. Tartu, 2007.
53. **Aleksei Krasnikov.** Luminescence and defects creation processes in lead tungstate crystals. Tartu, 2007.
54. **Küllike Rägo.** Superconducting properties of MgB_2 in a scenario with intra- and interband pairing channels. Tartu, 2008.
55. **Els Heinsalu.** Normal and anomalously slow diffusion under external fields. Tartu, 2008.
56. **Kuno Kooser.** Soft x-ray induced radiative and nonradiative core-hole decay processes in thin films and solids. Tartu, 2008.
57. **Vadim Boltrushko.** Theory of vibronic transitions with strong nonlinear vibronic interaction in solids. Tartu, 2008.
58. **Andi Hektor.** Neutrino Physics beyond the Standard Model. Tartu, 2008.
59. **Raavo Josepson.** Photoinduced field-assisted electron emission into gases. Tartu, 2008.
60. **Martti Pärs.** Study of spontaneous and photoinduced processes in molecular solids using high-resolution optical spectroscopy. Tartu, 2008.
61. **Kristjan Kannike.** Implications of neutrino masses. Tartu, 2008.
62. **Vigen Issahhanjan.** Hole and interstitial centres in radiation-resistant MgO single crystals. Tartu, 2008.
63. **Veera Krasnenko.** Computational modeling of fluorescent proteins. Tartu, 2008.
64. **Mait Müntel.** Detection of doubly charged higgs boson in the CMS detector. Tartu, 2008.
65. **Kalle Kepler.** Optimisation of patient doses and image quality in diagnostic radiology. Tartu, 2009.
66. **Jüri Raud.** Study of negative glow and positive column regions of capillary HF discharge. Tartu, 2009.
67. **Sven Lange.** Spectroscopic and phase-stabilisation properties of pure and rare-earth ions activated ZrO_2 and HfO_2. Tartu, 2010.
68. **Aarne Kasikov.** Optical characterization of inhomogeneous thin films. Tartu, 2010.
69. **Heli Valtna-Lukner.** Superluminally propagating localized optical pulses. Tartu, 2010.

70. **Artjom Vargunin.** Stochastic and deterministic features of ordering in the systems with a phase transition. Tartu, 2010.
71. **Hannes Liivat.** Probing new physics in e+e− annihilations into heavy particles via spin orientation effects. Tartu, 2010.
72. **Tanel Mullari.** On the second order relativistic deviation equation and its applications. Tartu, 2010.
73. **Aleksandr Lissovski.** Pulsed high-pressure discharge in argon: spectroscopic diagnostics, modeling and development. Tartu, 2010.
74. **Aile Tamm.** Atomic layer deposition of high-permittivity insulators from cyclopentadienyl-based precursors. Tartu, 2010.
75. **Janek Uin.** Electrical separation for generating standard aerosols in a wide particle size range. Tartu, 2011.
76. **Svetlana Ganina.** Hajusandmetega ülesanded kui üks võimalus füüsikaõppe efektiivsuse tõstmiseks. Tartu, 2011
77. **Joel Kuusk.** Measurement of top-of-canopy spectral reflectance of forests for developing vegetation radiative transfer models. Tartu, 2011.
78. **Raul Rammula**. Atomic layer deposition of HfO_2 – nucleation, growth and structure development of thin films. Tartu, 2011.
79. **Сергей Наконечный.** Исследование электронно-дырочных и интерстициал-вакансионных процессов в монокристаллах MgO и LiF методами термоактивационной спектроскопии. Тарту, 2011.
80. **Niina Voropajeva.** Elementary excitations near the boundary of a strongly correlated crystal. Tartu, 2011.
81. **Martin Timusk.** Development and characterization of hybrid electro-optical materials. Tartu, 2012, 106 p.
82. **Merle Lust.** Assessment of dose components to Estonian population. Tartu, 2012, 84 p.
83. **Karl Kruusamäe.** Deformation-dependent electrode impedance of ionic electromechanically active polymers. Tartu, 2012, 128 p.
84. **Liis Rebane.** Measurement of the $W \to \tau\nu$ cross section and a search for a doubly charged Higgs boson decaying to τ-leptons with the CMS detector. Tartu, 2012, 156 p.
85. **Jevgeni Šablonin.** Processes of structural defect creation in pure and doped MgO and NaCl single crystals under condition of low or super high density of electronic excitations. Tartu, 2013, 145 p.
86. **Riho Vendt**. Combined method for establishment and dissemination of the international temperature scale. Tartu, 2013, 108 p.
87. **Peeter Piksarv.** Spatiotemporal characterization of diffractive and non-diffractive light pulses. Tartu, 2013, 156 p.
88. **Anna Šugai.** Creation of structural defects under superhigh-dense irradiation of wide-gap metal oxides. Tartu, 2013, 108 p.
89. **Ivar Kuusik.** Soft X-ray spectroscopy of insulators. Tartu, 2013, 113 p.
90. **Viktor Vabson**. Measurement uncertainty in Estonian Standard Laboratory for Mass. Tartu, 2013, 134 p.

91. **Kaupo Voormansik.** X-band synthetic aperture radar applications for environmental monitoring. Tartu, 2014, 117 p.
92. **Deivid Pugal.** hp-FEM model of IPMC deformation. Tartu, 2014, 143 p.
93. **Siim Pikker.** Modification in the emission and spectral shape of photostable fluorophores by nanometallic structures. Tartu, 2014, 98 p.
94. **Mihkel Pajusalu**. Localized Photosynthetic Excitons. Tartu, 2014, 183 p.
95. **Taavi Vaikjärv.** Consideration of non-adiabaticity of the Pseudo-Jahn-Teller effect: contribution of phonons. Tartu, 2014, 129 p.
96. **Martin Vilbaste.** Uncertainty sources and analysis methods in realizing SI units of air humidity in Estonia. Tartu, 2014, 111 p.
97. **Mihkel Rähn.** Experimental nanophotonics: single-photon sources- and nanofiber-related studies. Tartu, 2015, 107 p.
98. **Raul Laasner.** Excited state dynamics under high excitation densities in tungstates. Tartu, 2015, 125 p.
99. **Andris Slavinskis.** EST Cube-1 attitude determination. Tartu, 2015, 104 p.
100. **Karlis Zalite**. Radar Remote Sensing for Monitoring Forest Floods and Agricultural Grasslands. Tartu, 2016, 124 p.
101. **Kaarel Piip.** Development of LIBS for *in-situ* study of ITER relevant materials. Tartu, 2016, 93 p.
102. **Kadri Isakar.** ^{210}Pb in Estonian air: long term study of activity concentrations and origin of radioactive lead. Tartu, 2016, 107 p.
103. **Artur Tamm.** High entropy alloys: study of structural properties and irradiation response. Tartu, 2016, 115 p.